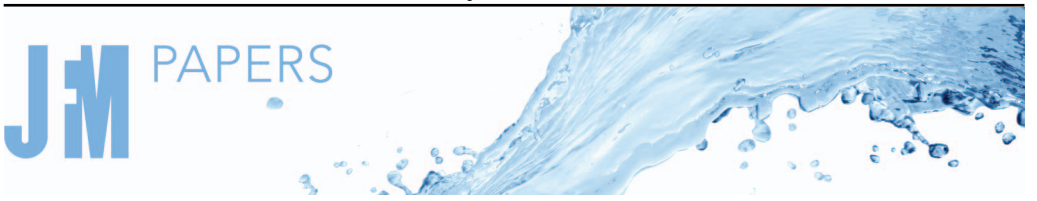
J. Fluid Mech. (2026), *vol.* 1033, A36, doi:10.1017/jfm.2025.11013



Multiscale understanding of explosion-induced particle jetting

Lvlan Miao[1,†], **Min Lin**[1,†], **Jiarui Li**[2], **Chuan-Yu Wu**[3], **Binfeng Sun**[4] and **Kun Xue**[1]

[1]Beijing Institute of Technology, Beijing 100081, PR China

[2]Institute of Applied Physics and Computational Mathematics, Beijing 1000871, PR China

[3]School of Chemistry and Chemical Engineering, University of Surrey, Guildford GU2 7XH, UK

[4]Engineering and Safety Technology Research Institute, NORINCO, Beijing 1000871, PR China

Corresponding author: Kun Xue, xuekun@bit.edu.cn

(Received 27 May 2025; revised 25 October 2025; accepted 28 November 2025)

The explosive dispersal of granular media, exemplified by the rapid radial expansion of a dense particle ring driven by internal pressurised gases, serves as a paradigmatic system for investigating multiphase blast dynamics. Despite the ubiquity of jetting and clustering phenomena in explosive dispersal scenarios, their governing mechanisms remain poorly resolved. In this work, we combine compressible computational fluid dynamics–discrete parcel method simulations, and theoretical modelling to elucidate the multiscale physics underlying explosion-induced particle jetting. We reveal a hierarchy of jetting structures, comprising non-jetting, suppressed jetting and prominent jetting, which are governed by the interplay between microscale particle force-chain evolution, mesoscale gas–particle coupling and macroscale ring dynamics. Jetting initiation emerges from the transient competition between shock-induced particle compaction and gas filtration during the early expansion phase, whereas sustained jet development requires subsequent ring implosion driven by adverse pressure gradients. By unifying this multiscale dynamics, we reduce the system's complexity into two dimensionless parameters: one characterising mesoscale gas–particle interactions and another quantifying macroscale implosion intensity. A phase diagram for jetting morphology under weak-shock conditions is established in this dimensionless parameter space, delineating two necessary criteria for jet formation. Systems failing either criterion exhibit no jetting, resolving long-standing ambiguities in the prediction of explosive dispersal structures.

Key words: shock waves, mixing enhancement, particle/fluid flow

[†] first author.

© The Author(s), 2026. Published by Cambridge University Press.

https://doi.org/10.1017/jfm.2025.11013 Published online by Cambridge University Press

1. Introduction

The explosive dispersal of granular media, driven by the detonation of a central high explosive (HE) or the sudden release of pressurised gases, transforms densely packed particle assemblies into dilute particle clouds. This phenomenon spans diverse natural and engineering systems. For instance, in volcanic eruptions, the explosive expansion of pressurised gases expels mixtures of gas and pyroclastic fragments through volcanic conduits (Narbona-Reina *et al.* 2024). In engineered systems, such as explosively dispersed dry-powder fire extinguishers (Haoyang & Du 2024), thermobaric weapons (Ritzel *et al.* 1888; Türker 2016) and fuel-air bombs (Zhang *et al.* 2015; Bai *et al.* 2018; Chen, Wang & Liu 2020), the dispersal efficiency of granular media and subsequent mixing kinetics with ambient air are critical for reliable performance. Emergent structures, such as particle jets or clusters, govern mass and momentum transfer between particles and gases, ultimately determining the spatial distribution and concentration of the resulting aerosol cloud (Gregoire 2012; Frost *et al.* 2012; Frost 2018). Moreover, the formation of such structures signifies the emergence of multiphase flow instabilities. However, the governing mechanisms are not fully understood and are a subject of ongoing research (Milne *et al.* 2014; Ripley & Zhang 2014; Frost *et al.* 2017; Koneru *et al.* 2020; Miao, Li & Xue 2024). For instance, in strong blast regimes, studies have demonstrated that the jetting observed on a short time scale cannot be attributed to classical hydrodynamic instabilities, like the Richtmyer–Meshkov or Rayleigh–Taylor instability, which develop over longer periods (Milne *et al.* 2014).

It has been widely observed that particle clusters or aggregates with characteristic dimensions orders of magnitude larger than individual particles are propelled outward during explosive dispersal in both strong blast loadings (Milne *et al.* 2014; Frost *et al.* 2017; Loiseau *et al.* 2018; Pontalier *et al.* 2018) induced by HEs as well as in the weak-shock impingement generated by the sudden release of central pressurised gases (Rodriguez *et al.* 2013, 2014, 2017; Xue *et al.* 2018; Yoo, Kim & Kim 2025). In the strong blast scenario, the loading is sufficiently high that blast-compacted ductile powders, such as aluminium, can attain densities approaching that of solid aluminium (Borg & Vogler 2008; Borg & Vogler 2013). High-speed radiography (Frost *et al.* 2017) reveals that jet initiation coincides with crack propagation within the compacted layer, initiated by the reflected tensile waves from the outer surface. This shell fragmentation theory also applies to brittle particulate systems like glass beads, which consolidate into compacts after undergoing severe blast-induced pulverisation and transiently behave as cohesive shells (Milne *et al.* 2014). Notably, blast dispersal experiments often involve the detonation of an electric detonator, which produces extremely high local pressures and highly directional jets of detonation products that may well account for the observed particle jets (Ripley & Zhang 2014).

By contrast, the explosive dispersal of particle rings confined in a horizontal Hele-Shaw cell and subjected to the sudden release of central pressurised gases constitutes a quasi-two-dimensional and axisymmetric configuration. This set-up excludes particle deformation, fracture and potential solidification due to markedly lower pressures ($\sim 10^0$–10^1 bar). Consequently, the dispersal structures arising from weak-shock impingement have been the focus of recent works. Rodriguez *et al.* reported both internal and external particle jets with distinct morphologies and wavelengths, finding that the number of internal jets increases with the shock wave Mach number. The evolution of this dual jetting was also quantified by Xue *et al.* (2018), who proposed a quadratic growth law for external jets. Yoo *et al.* (2025) further revealed the non-trivial role of particle cohesion and size on the morphology of the finger structure at the inner boundary.

For thin particle rings, internal jetting dominates the dispersal pattern, while external jetting defines the pattern for thick rings (Yoo *et al.* 2025). The finger-like internal jetting is

https://doi.org/10.1017/jfm.2025.11013 Published online by Cambridge University Press

often attributed to the Saffman–Taylor instability. As for the external particle jetting, many researchers (Balakrishnan 2014; Osnes, Vartdal & BA 2018; Chiapolino & Saurel 2020; Koneru *et al.* 2020) attribute this phenomenon to a shock-driven multiphase instability (SDMI) (Vorobieff *et al.* 2011), analogous to the classical Richtmyer–Meshkov instability. In this framework, as the post-shock gases flow through particles, the reduction of gas velocity caused by particle–gas momentum exchange serves as the primary driver of SDMI. For sustained instability growth, the gas–particle velocity equilibration time scale (t_v) must be smaller than or comparable to the characteristic hydrodynamic time scale (Duke-Walker *et al.* 2021; Ouellet *et al.* 2022). In dilute gas–particle flows, t_v scales as the square of particle diameter multiplied by particle density, $t_v \propto d_p^2 \rho_p$, implying that SDMI develops prominently only in systems laden with micron- or submicron-sized lightweight particles (Daniel & Wagner 2022). Larger or denser particles lag significantly behind the carrier gas, thereby suppressing the instability's growth. Furthermore, the predominance of dense gas–particle mixtures during the initial jet development phase precludes instantaneous momentum equilibrium (Demauro *et al.* 2019; Bajpai *et al.* 2025), thereby limiting the applicability of the SDMI in the weak-shock regime.

Despite recent advances, the fundamental physics governing the formation of particle jets in explosive dispersal remains unclear. A particular challenge is predicting how the diversity of jetting patterns relates to the structural parameters of the dispersal system, especially under weak-shock conditions. To address this, we conduct a systematic numerical investigation across a broad parametric space. This work extends the framework of our prior studies (Xue *et al.* 2023; Miao *et al.* 2024), employing the same coarse-grained computational fluid dynamics–discrete parcel method (CFD-DPM) framework (Tian *et al.* 2020) and a prototypical annular particle shell configuration. This methodological consistency ensures the comparability of results and a reliable analysis of parametric effects.

While our previous research identified distinct global dispersal modes governed by multiscale gas–particle coupling, it did not resolve the internal structure of the dispersal cloud. Here, we shift focus to the underlying jetting morphology. We demonstrate that jet initiation and evolution are governed by a hierarchical interplay across the micro-, meso- and macro-scales. This insight allows us to establish physical criteria for jetting and introduce new dimensionless parameters that consolidate these cross-scale dynamics. These parameters enable the construction of a phase diagram for the jetting morphology in the weak-shock regime. Furthermore, we show that these critical parameters can be derived from a refined continuum model, enabling the *a priori* prediction of jetting patterns.

The paper is organised as follows: Section 2 details the numerical methods. Sections 3 and 4 analyse the transitions of jetting morphology, the governing dynamics, the proposed criteria and the predictive model. Section 5 concludes with a summary and broader implications.

2. Numerical method

2.1. *Governing equations and numerical algorithm*

Numerical simulations employ CCFD-DPM, a coarse-grained Euler–Lagrange numerical approach suitable for gas–particle flows in laboratory-scale systems (Tian *et al.* 2020). This method explicitly resolves parcel–parcel contact forces, where each computational parcel represents an ensemble of physical particles sharing identical physical and kinematic properties. The number of real particles per parcel is quantified by the super-particle loading factor, χ, determined by the particle volume fraction and computational

https://doi.org/10.1017/jfm.2025.11013 Published online by Cambridge University Press

constraints. For particle–gas systems, the reported χ in previous literature ranges from $O(10^1)$ to $O(10^3)$(Osnes *et al.* 2018; Koneru *et al.* 2020). In the present work, χ is of the order of $O(10^1)$.

The gas-phase dynamics is governed by volume-averaged Eulerian equations (2.1)–(2.3), derived from a simplified five-equation transport model based on the Baer–Nunziato (BN) model (Baer & Nunziato 1986). This formulation extends the BN model to simulate compressible multiphase flows across dilute-to-dense gas–particle regimes

$$\frac{\partial \left(\phi_f \left\langle \rho_f \right\rangle\right)}{\partial t} + \nabla \cdot \left(\phi_f \left\langle \rho_f \right\rangle \tilde{\boldsymbol{u}}_f\right) = 0, \tag{2.1}$$

$$\begin{aligned}\frac{\partial \left(\phi_f \tilde{\boldsymbol{u}}_f \left\langle \rho_f \right\rangle\right)}{\partial t} &+ \nabla \cdot \left(\phi_f \left\langle \rho_f \right\rangle \tilde{\boldsymbol{u}}_f \tilde{\boldsymbol{u}}_f + \phi_f \left\langle P_f \right\rangle\right) \\ &= \left\langle P_f \right\rangle \nabla \phi_f + \sum_i \left\{\phi_{p,i} \rho_{p,i} D_{p,i} \left(\tilde{\boldsymbol{u}}_{p,i} - \left(\tilde{\boldsymbol{u}}_f\right)_i\right)\right\},\end{aligned} \tag{2.2}$$

$$\begin{aligned}\frac{\partial \left(\phi_f \left\langle \rho_f \right\rangle \tilde{E}_f\right)}{\partial t} &+ \nabla \cdot \left(\phi_f \left\langle \rho_f \right\rangle \tilde{E}_f \tilde{\boldsymbol{u}}_f + \phi_f \left\langle p_f \right\rangle \tilde{\boldsymbol{u}}_f\right) \\ &= \left\langle P_f \right\rangle \nabla \phi_f \cdot \tilde{\boldsymbol{u}}_p + \sum_i \left\{\phi_{p,i} \rho_{p,i} D_{p,i} \left(\boldsymbol{u}_{p,i} - \left(\tilde{\boldsymbol{u}}_f\right)_i\right) \cdot \tilde{\boldsymbol{u}}_{p,i}\right\}.\end{aligned} \tag{2.3}$$

The gas-phase variables include the volume fraction (ϕ_f), density (ρ_f), velocity ($\boldsymbol{u}_f$), pressure (P_f) and the total energy (E_f), where $E_f = \rho_f \cdot e_f + 0.5\ \rho_f \cdot \boldsymbol{u}_f^2$. In (2.1)–(2.3), $\langle\rangle$ and $\tilde{}$ denote phase-averaged and mass-averaged variables, respectively. For the particle phase, $\rho_{p.i}$ and $\boldsymbol{u}_{p,i}$ represent the density and velocity of parcel i, while $D_{p,i}$ is the drag force coefficient. The contribution of parcel i to the weighted particle volume fraction is defined as $\phi_{p.i} = w_{i,f}\ V_{p,i}\ /V_f$, where $w_{i,f}$ is the distributed weight of parcel i in fluid cell f, and $V_{p,i}$ and V_f are the volumes of parcel and the fluid cell, respectively.

The drag coefficient D_p is computed using the Di Felice model coupled with Ergun's equation ((2.4)–(2.6)) (Di Felice 1994), which accounts for the particle Reynold number (Re_p) and the particle-phase volume fraction (ϕ_p) and has been widely used in particle-laden multiphase flows

$$D_p = 0.75 C_d Re_p \phi_f^{1-\beta}, \tag{2.4}$$

where C_d is the drag coefficient proposed by Dallavalle

$$C_d = \left(0.63 + \frac{4.8}{\sqrt{\phi_f Re_p}}\right)^2. \tag{2.5}$$

The exponent in (2.4) is not constant but a function of Re_p

$$\beta = 3.7 - 0.65 \exp\left(-\frac{(1.5 - \lg(\phi_f Re_p))^2}{2}\right). \tag{2.6}$$

The continuous formulation of the Di Felice (1994) drag model ensures numerical stability across the wide range of solid volume fractions encountered during the transition from dense compaction to dilute dispersal. While more recent models derived from particle-resolved simulations offer refined correlations for specific configurations (Beetstra, Hoef & Kuipers 2007; Tenneti, Garg & Subramaniam 2011) and some incorporate finite Mach number effects and unsteady forces (Parmar, Haselbacher &

https://doi.org/10.1017/jfm.2025.11013 Published online by Cambridge University Press

Balachandar 2009; Ling, Parmar & Balachandar 2013), they are, of necessity, regime-dependent. For the present weak-shock conditions, characterised by subsonic interstitial flows where Mach number corrections are negligible (Duke-Walker *et al.* 2021) and there are high particle Reynolds numbers in the post-transient phase, the Di Felice model provides a well-established and physically sound representation of the quasi-steady drag force. This force is the dominant component governing the momentum exchange central to the jetting dynamics under investigation (Mehta *et al.* 2018; Osnes *et al.* 2020).

To ensure the applicability of the three-dimensional drag correlation in our two-dimensional simulation, the local two-dimensional porosity calculated from the disk assembly is converted to an equivalent three-dimensional porosity using an established geometric mapping (Zhang *et al.* 2010). This conversion is based on a linear interpolation between the theoretical maximum and minimum packing densities for mono-sized disks and spheres. The equivalent three-dimensional (3-D) porosity, $\phi_{3\text{-D}}$, is calculated as follows:

$$\phi_{3-\mathrm{D}} = 0.2595 + \frac{\phi_{2-\mathrm{D}} - 0.0931}{0.2146 - 0.0931}(0.4760 - 0.2595), \tag{2.7}$$

where the numerical constants correspond to the extreme packing states in two and three dimensions. This equivalent $f_{3\text{-D}}$ is then used as the input for the Di Felice drag model. All particle-scale properties, such as mass and contact stiffness, are defined with consistent 2-D units.

The particle phase is modelled as discrete parcels governed by Newton's second law ((2.8) and (2.9))

$$\frac{\mathrm{d}u_{p,i}}{\mathrm{d}t} = D_{p,i}\left(\boldsymbol{u}_f - \boldsymbol{u}_{p,i}\right) - \frac{1}{\rho_p}\nabla\left\langle P_f\right\rangle + \frac{1}{m_p}\sum_j \boldsymbol{F}_{C,ij}, \tag{2.8}$$

$$\frac{\mathrm{d}x_{p,i}}{\mathrm{d}t} = \boldsymbol{u}_{p,i}, \tag{2.9}$$

where $\boldsymbol{u}_{p,i}$ and $\boldsymbol{x}_{p,i}$ are the velocity and displacement of parcel i, respectively, and $\boldsymbol{F}_{C,ij}$ represents the collision force between parcels i and j.

A four-way coupling scheme integrates the momentum and energy exchange between the gas and particle phases. The gas-phase momentum and energy equations include source terms from the particle drag force and the associated work. Conversely, parcels are influenced by the gas-phase pressure gradients, drag forces and inter-parcel collisions ((2.8)). Collision forces $\boldsymbol{F}_{C,ij}$ are modelled using a linear-spring dashpot model, comprising a repulsive spring force and a velocity-proportional damping force

$$\boldsymbol{F}_{C,ij} = k_{n,p}\delta_n - \gamma_{n,p}\boldsymbol{u}_{n,ij}, \tag{2.10}$$

where $k_{n,p}$ and $\gamma_{n,p}$ are the stiffness and damping coefficients of the parcels, δ_n is the overlap between colliding parcels and $\boldsymbol{u}_{n,ij}$ is their relative normal velocity. The normal contact stiffness, $k_{n,p}$, is not an arbitrary parameter but scales with the equivalent Young's modulus, $E*$, under a plane-strain assumption

$$k_{n,p} = \frac{\pi}{4}E^*L, \tag{2.11}$$

where L is the thickness of the disks, taken as unity in our 2-D simulation. For two identical discs with Young's modulus Y and Poisson's ratio v, the equivalent Young's modulus is given by $E^* = Y/1 - v^2$. For the soda-lime glass spheres primarily simulated, we calculated $k_{n,p}$ based on Young's modulus (78 GPa) and Poisson's ratio (0.22).

https://doi.org/10.1017/jfm.2025.11013 Published online by Cambridge University Press

The damping coefficient $\gamma_{n,p}$ is derived from the restitution coefficient ϵ_p of the parcels

$$\gamma_{n,p} = -\frac{2\ln\varepsilon_p}{\sqrt{\pi^2 + \ln\varepsilon_p}}\sqrt{m_p k_{n,p}}. \tag{2.12}$$

The restitution coefficient, ϵ_p, which governs energy dissipation during collisions, was set to 0.95. This value was calibrated to match the particle dispersion velocities predicted by the Gurney model and reference direct numerical simulation data (Zhang, Feng & Xue 2023).

The normal stiffness $k_{n,p}$ and restitution coefficient ϵ_p are critical parameters governing the inter-particle momentum transfer and the resulting force-chain network. While the present study employs values calibrated for the specific materials under investigation, these micromechanical properties are known to significantly influence the macroscopic response, such as the propagation speed of the compaction front and the heterogeneity of the force network. The potential coupling between these contact properties and the observed jetting morphologies thus remains a compelling aspect for further exploration.

In the present simulations, the characteristic length of the fluid cells was maintained within a range of 1.5–2 times the particle diameter across all cases. This grid resolution has been demonstrated to be sufficient for capturing the dominant gas–particle coupling dynamics in similar dense, shock-driven flows (Miao *et al.* 2024; Han & Xue 2025).

The gas-phase governing equations are solved using weighted essentially no oscillatory scheme for spatial reconstruction of flow variables. Intercell fluxes are computed via the Harten–Lax–van Leer Riemann solver, and time integration is performed with a third-order Runge–Kutta method. Parcel trajectories are advanced using the velocity-Verlet algorithm, while bilinear or trilinear interpolation maps particle volume fractions, source terms and fluid variables between Eulerian grids and Lagrangian parcels (Liu, Osher & Chan 1994). Further numerical details of the CCFD-DPM framework can be found in our prior works (Tian *et al.* 2020).

The CCFD-DPM framework has been rigorously validated against benchmark experiments involving shock-driven particle-laden flows (Tian *et al.* 2020), including shock dissipation through particle curtains (Rogue's experiments) (Rogue *et al.* 1998), gas- and solid-phase pressure dynamics in shock-impinged particle columns (experiments performed by Britan and Ben-Dor) (Britan & Ben-Dor 2006), shock-induced dispersion of thin particle curtains (shock tube experiments performed by Wagner *et al.*) (Wagner *et al.* 2012; Han & Xue 2025) and the shock-induced interfacial instability of granular media (Xue *et al.* 2018). Notably the CCFD-DPM simulations reproduce the characteristic expanding velocity and finger-like jetting structures observed during explosive dispersal of granular materials (Xue *et al.* 2023), corroborating its capability to resolve multiphase interaction in high-speed, dense regimes.

2.2. *Numerical set-up*

The 2-D numerical configuration is illustrated in figure 1(*a*). A high-pressure gas pocket (initial pressure P_0, radius R_{gas}) is enclosed by a densely packed annular particle ring with initial inner and outer radii $R_{in,0}$ and $R_{out,0}$, respectively. The particle ring is populated with computational parcels generated via a radius expansion algorithm. Regions outside the particle ring and inter-particle pores (excluding the central gas pocket) are initialised with ambient air. To construct the particle assembly, an initial population of parcels with artificially reduced radii (to prevent overlap) is randomly distributed. These parcels are iteratively expanded until the target size distribution and packing fraction (ϕ_0) are achieved. Real particles have a diameter d_p, while computational parcel diameters are

https://doi.org/10.1017/jfm.2025.11013 Published online by Cambridge University Press

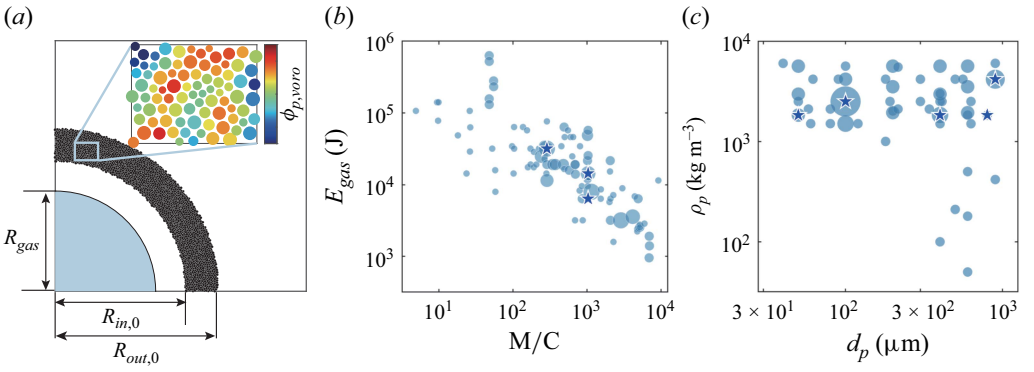


Figure 1. (*a*) Two-dimensional numerical configuration of explosive dispersal of particle ring. (*b*)–(*c*) Distribution of numerical cases across the (E_{gas}, *M*/*C*) (*b*) and (d_p, r_p) (*c*) parameter spaces. Symbol sizes in (*b*) and (*c*) scale with the occurrence frequency of each (d_p, r_p) combination across all numerical cases, key numerical cases are marked with star symbols, which correspond to the representative examples presented in detail within figures 3 and 4.

uniformly distributed between 0.75 d_p and 1.25 d_p to suppress crystallisation during shock compaction. Parcels are arranged randomly yet homogeneously, as shown in the zoomed-in inset of figure 1(*a*), where colours represent the local Voronoi-based packing fraction ($\phi_{p,voro}$). Each parcel retains the material density (ρ_p) of real particles.

Prior studies indicate that macro- and microscale parameters jointly influence dispersal behaviour, albeit with varying significance (Miao *et al.* 2024). To decouple their effects on jetting morphology, over 140 numerical cases were simulated, spanning wide ranges of macro- and microscale parameters. Macroscale parameters include the gas pocket explosion energy E_{gas}, approximated by using the Brode equation (Crowl 2003)

$$E_{gas} = \frac{(P_0 - P_{amb})\, V_{gas}}{\gamma - 1} = \frac{\pi\, (P_0 - P_{amb})\, R_{gas}^2}{\gamma - 1}, \tag{2.13}$$

where V_{gas} is the gas pocket volume, P_{amb} is the ambient pressure and γ is the specific heat ratio. The mass-to-charge ratio, *M*/*C*, is defined as

$$\frac{M}{C} = \frac{\pi \left(R_{out,0}^2 - R_{in,0}^2\right) \phi_0 \rho_p}{\pi\, R_{gas}^2 \rho_f} = \frac{\left(R_{out,0}^2 - R_{in,0}^2\right) \phi_0 \rho_p R T_0}{R_{gas}^2 P_0}, \tag{2.14}$$

where ρ_f is the gas density. Microscale parameters encompass particle diameter d_p and material density ρ_p. The distribution of cases across the (E_{gas}, *M*/*C*) and (d_p, ρ_p) parameter spaces is shown in figures 1(*b*) and 1(*c*), respectively. Symbol sizes in figures 1(*b*) and 1(*c*) scale with the occurrence frequency of each (d_p, ρ_p) combination across all numerical cases.

As indicated in figure 1(*b*), *M*/*C* spans five orders of magnitude, from $O(10^0)$ to $O(10^4)$. Particle diameter d_p ranges from $O(10^1)$ to $O(10^2)$ μm, while ρ_p varies over two decades between minimum and maximum values. This broad parameter space enables systematic exploration of dispersal behaviour variability, which is challenging to achieve experimentally. Structural parameters for all cases are tabulated in table 1 (Appendix A. For clarity, each case is labeled as, M/C, -ϕ_0, -d_p (in units of μm), -ρ_p (in units of kg m^{-3})).

https://doi.org/10.1017/jfm.2025.11013 Published online by Cambridge University Press

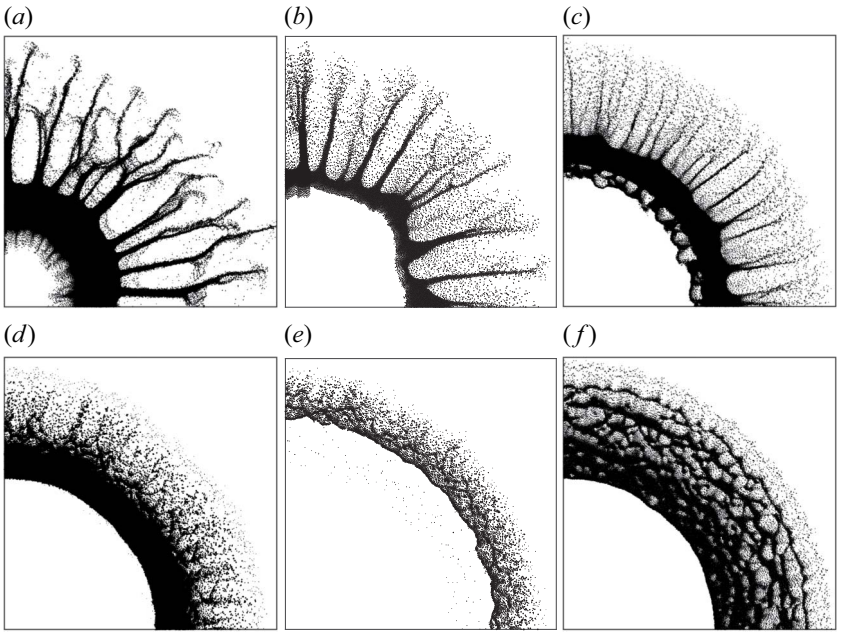


Figure 2. Contours of jetting morphologies in different numerical cases: (*a*) 1035-0.6-50-1828, (*b*) 1035-0.6-100-2500, (*c*) 1035-0.6-400-1828, (*d*) 1035-0.6-800-1828, (*e*) 287-0.5-900-4167, (*f*) 1014-0.5-400-1828.

3. Results

3.1. *Diverse jetting morphologies*

Numerical simulations illustrate the complex dependence of jetting morphology on system parameters. Figure 2(*a*)–(*f*) shows a progressive transition across cases. Well-defined, thick branched jets dominate in case 1035-0.6-50-1828 (figure 2*a*), transitioning to slender spikes with fuzzy tips in case 1035-0.6-100-2500 (figure 2*b*) and further evolving into flimsy ligaments in case 1035-0.6-400-1828 (figure 2*c*). Non-jetting patterns emerge in cases 1035-0.6-800-1828, 287-0.5-900-4167, 1014-0.5-400-1828 (figure 2*d–f*), where dispersed particles form diffuse or cellular layers. This morphological transition manifests how the multiscale interplay of M/C, volume fraction (ϕ_0), ρ_p and d_p vary in the jetting dynamics.

The simulated r–t diagrams of the circumferentially averaged particle volume fraction, $\phi_p(r,t)$, reveal the dispersion process and jetting evolution, as illustrated in figure 3(*a*)–(*f*). Here, the inner and outer surfaces of particle clouds are defined by radii of R_{in} and R_{out}, respectively, such that only 5 % of particles reside inside R_{in} or outside R_{out}. The inner and outer boundaries of a densely packed annular region ($\phi_p > 0.3$) are identified by radii $R_{in,dense}$ and R_{dense}, respectively. Beyond $R_{out,dense}$ particles either form jets or diffuse. The jet length is defined as $l_{jet} = R_{out} - R_{dense}$. Temporal variations in R_{in}, R_{out}, $R_{in,dense}$ and R_{dense} are overlaid on the $\phi_p(r$–$t)$ diagrams.

Figure 3(*a*)–(*f*) exhibits a diverse dynamics of the particle ring, ranging from consistent expansion (figure 3*e*), to retention following an initial expansion (figure 3*c*,*d*,*f*) and persistent expansion–implosion cycles (figure 3*a*,*b*). Notably, cases 1035-0.6-50-1828, 1035-0.6-100-2500 (figures 3*a* and 3*b*), which correspond to systems with the most prominent jetting patterns (see figures 2*a* and 2*b*), display strong cyclic behaviour. In contrast, jetting is significantly suppressed in case 1035-0.6-400-1828 (figure 2*c*), where

https://doi.org/10.1017/jfm.2025.11013 Published online by Cambridge University Press

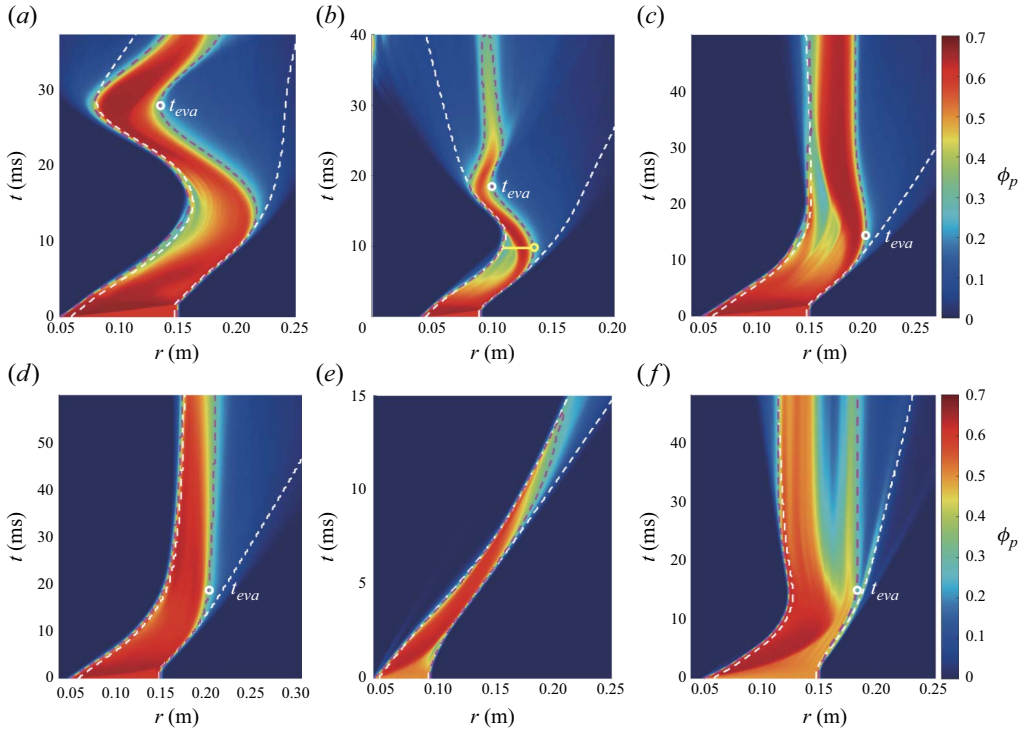


Figure 3. Simulated r–t diagrams of $\phi_p(r,t)$ in cases 1035-0.6-50-1828 (a), 1035-0.6-100-2500 (b), 1035-0.6-400-1828 (c), 1035-0.6-800-1828 (d), 287-0.5-900-4167 (e), 1014-0.5-400-1828 (f). The superimposed trajectories are (from left to right): the inner surface of the cloud (R_{in}), inner and outer surfaces of the densely packed ring ($R_{in,dense}$, R_{dense}) and outer surface of the cloud (R_{out}). The evaluating time for jetting, t_{eva}, is marked by white circle symbols in R_{dense} trajectories.

structures are reduced to flimsy filaments. Figure 3(d–f) corresponds to non-jetting systems characterised by monotonic expansion or an expansion–retention dynamics.

Notably, the parameter combination, rather than a single parameter, varies from case to case in figures 2 and 3. This choice is made to manifest the combined influences of the multitude of parameters, which collectively govern the multiscale gas–particle coupling processes that will be elaborated upon in § 3.5. To systematically discern the effect of individual parameters, a comparative analysis of cases where only one parameter is varied while others are held constant is provided in Appendix A.

Critically, the evolution of jetting patterns is not consistent with a monotonic progression in the particle dynamics. While correlations exist – such as enhanced jetting in systems with cyclic expansion–implosion – no explicit relationship is observed. For instance, jet suppression in case 1035-0.6-400-1828 (figure 2c) occurs despite similarities in the particle retention dynamics to jetting systems (figure 3c). This implies that jet formation depends on additional factors beyond bulk ring behaviour, such as microscale particle dynamics and mesoscale gas–particle coupling.

The growth of normalised jet length, $\hat{l}_{jet}$, $\hat{l}_{jet}(t) = l_{jet}(t)/R_{dense}(t)$, for jetting systems 1035-0.6-50-1828 (a), 1035-0.6-100-2500 (b), 1035-0.6-400-1828 (c), alongside the normalised expansion velocity of densely packing ring $\hat{V}_{dense}(t)$, $\hat{V}_{dense}(t) = V_{dense}(t)/V_{Gurney}$, is shown in figure 4($a$–$c$). It is worth noting that $\hat{l}_{jet}$ undergoes accelerated growth as $\hat{V}_{dense}$ decreases. The most prominent growth occurs during the implosion of

https://doi.org/10.1017/jfm.2025.11013 Published online by Cambridge University Press

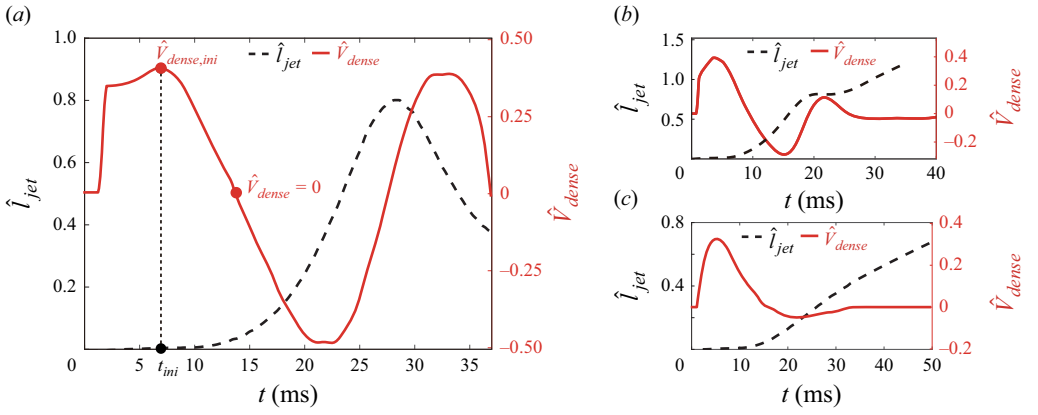


Figure 4. Temporal evolution of the normalised jet length, $\hat{l}_{jet} = l_{jet}(t) / R_{dense}(t)$, and normalised expansion velocity, $\hat{V}_{dense} = V_{dense}(t)/ V_{Gurney}$ for cases 1035-0.6-50-1828 (*a*), 1035-0.6-100-2500 (*b*), 1035-0.6-400-1828 (*c*). The $\hat{l}_{jet}(t)$ and $\hat{V}_{peak}(t)$ curves in (*a*) are annotated with two symbols marking the onset of decrease of $\hat{V}_{dense}$ and the initiation of ring implosion.

the densely packed ring marked by $\hat{V}_{dense} < 0$. Here, $\hat{l}_{jet}$ continues to grow until the ring collapses to its minimum radius with $\hat{V}_{dense} \sim 0$. Subsequently, $\hat{l}_{jet}$ either exhibits semi-linear growth (if the dense ring stagnates, $V_{dense} \sim 0$) (figure 4*c*) or begins to slightly decay (if the ring undergoes a second expansion, $\hat{V}_{dense} > 0$) (figure 4*b*).

3.2. *Characterisation of jetting intensity*

To systematically evaluate jetting patterns across diverse explosive dispersal systems within a universal framework, a robust method for characterising jetting intensity is necessary. In this section, we propose a descriptor to quantify the significance of circumferential particle clustering relative to the entire dispersed particle population. Due to the rapid morphological evolution of the particle cloud, selecting an appropriate measurement time is critical. As shown in figure 2, dispersed particles exhibit three distinct states: (i) compacted in the densely packed ring; (ii) diffusing inside the cavity bounded by a dense ring; (iii) ejected as jets or diffuse structures. Particles in the third category – hereafter termed jetting particles – are defined as those occupying regions between radii of R_{dense} and R_{out}.

For systems where the particle ring undergoes ring retention following an initial expansion (cases1035-0.6-400-1828, 1035-0.6-800-1828, 1014-0.5-400-1828) or persistent expansion–implosion cycles (cases 1035-0.6-50-1828 and 1035-0.6-100-2500), the evaluation time t*eva* is defined as the moment when the proportion of jetting particles, ϕ_{jettng}, reaches its maximum. Figure 5 illustrates the relationship between ϕ_{jettng} and R_{dense} for cases 1035-0.6-50-1828 (a), 1035-0.6-100-2500 (b), 1035-0.6-400-1828 (c), where the densely packed rings persist. Here, ϕ_{jettng} peaks when the rings collapse to their minimum radii. Subsequently, ϕ_{jettng} stabilises if the ring stagnates (figure 5*c*) or fluctuates synchronously with pulsations of the dense ring (figures 5*a* and 5*b*). Consequently, t_{eva} corresponds to the time when R_{dense} reaches its minimum after the initial expansion. For systems where the particle ring undergoes persistent expansion (case 287-0.5-900-4167), t_{eva} is selected as the time when the ring expands to ten times its initial radius, $R_{dense} = 10\, R_{out,0}$. The selected t_{eva} values are annotated in figure 3.

https://doi.org/10.1017/jfm.2025.11013 Published online by Cambridge University Press

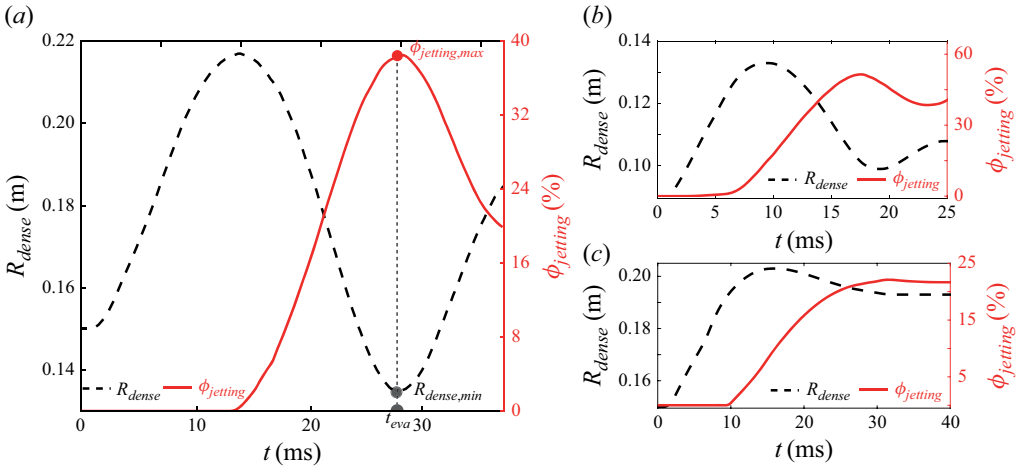


Figure 5. Temporal evolutions of ϕ_{jettng} and R_{dense} for cases 1035-0.6-50-1828 (a), 1035-0.6-100-2500 (b), 1035-0.6-400-1828 (c). The corresponding $\phi_{jettng,max}$ and $R_{dense,min}$ are marked in (a).

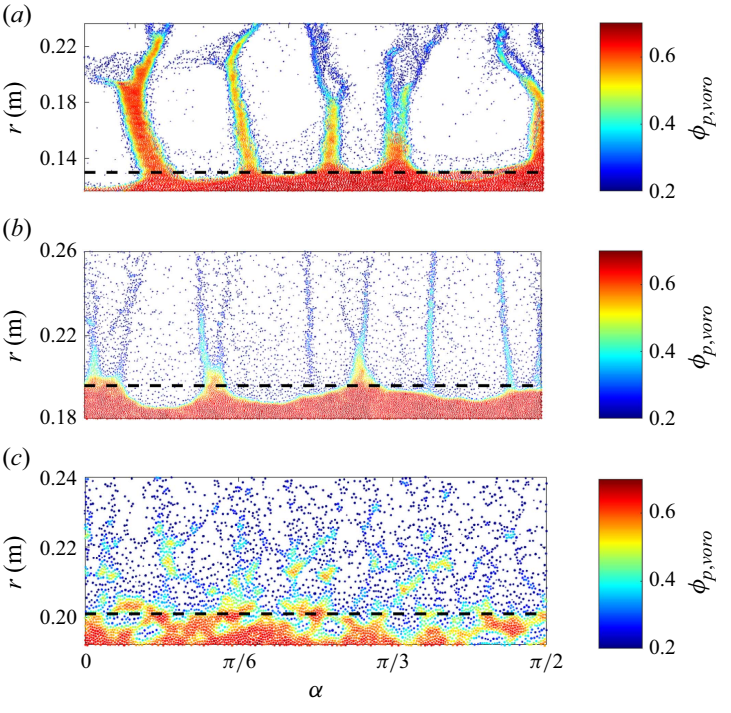


Figure 6. Spatial distributions of $\phi_{p,voro}$ of jetting particles within a one-eighth azimuthal sector ($0 < a < \pi/4$): (a) 1035-0.6-50-1828, (b) 1035-0.6-400-1828, (c)1035-0.6-800-1828; Horizontal dashed lines mark the outer boundary of densely packed rings (R_{dense}) in simulations.

To quantify particle clustering in the jetting region, we analyse Voronoi volume fractions ($\phi_{p,voro}$) from simulations. Figure 6(a)–(c) displays the spatial distributions of $\phi_{p,voro}$ for numerical cases (a) 1035–0.6-50–1828, (b) 1035–0.6-400–1828, (c) 1035–0.6-800–1828) of jetting particles within a one-eighth azimuthal sector ($0 < a < \pi/4$). Particles in jet

https://doi.org/10.1017/jfm.2025.11013 Published online by Cambridge University Press

stems exhibit elevated $\phi_{p,voro}$ whereas those in diffuse inter-jet regions show significantly lower values.

Based on $\phi_{p,voro}$, the jetting intensity descriptor, ω_{jet}, can be defined as

$$\omega_{jet} = \frac{\sqrt{\sum_{i=1}^{n}\left(\phi_{p,voro}^{i} - \phi_{p,min}\right)^2 / n}}{\phi_{p,min}} \cdot \varphi_{jetting} \quad \text{for simulations,} \tag{3.1}$$

where $\phi_{p,voro}^{i}$ represents the Voronoi volume fraction of the ith particle among n jetting particles for numerical cases The minima $\phi_{p,min}$ correspond to particle-sparse gaps between jets. The first term in (3.1) quantifies the deviation of local packing density from gap regions, while the second term weights the significance of jetting particles relative to the entire dispersed population. It is important to note that ω_{jet} is not designed to quantify the transient number or amplitude of individual jets. Instead, it integration over the jetting region characterises the fully realised jetting morphology, distinguishing systems where jetting is a dominant feature from those where it is suppressed or absent. The jetting intensity descriptor, ω_{jet}, provides a holistic measure of the significance of circumferential clustering in the dispersed cloud.

Consistent with (3.1) the jetting intensity descriptor ω_{jet} exhibits systematic trends across regimes. The value of ω_{jet} declines from 8.8 (case 1035-0.6-50-1828) and 3.9 (case 1035-0.6-100-2500) in jetting-dominated systems to 2.0 (case 1035-0.6-400-1828) in transitional states, and ultimately to 0.24 (case 1035-0.6-800-1828), 0.02 (case 287-0.5-900-4167) and 0.015 (case 1014-0.5-400-1828) in non-jetting configurations.

A three orders of magnitude difference in ω_{jet} distinguishes jetting ($\sim O(10^0)$) from non-jetting ($\sim O(10^{-2})$) systems, corroborating ω_{jet} robustness in quantifying jetting intensity and discriminating dispersed structures. Full numerical results for ω_{jet} are tabulated in table 1 in Appendix A.

3.3. *Jet initiation: micro particle dynamics and meso-scale gas–particle coupling*

As illustrated in figure 4, the pronounced growth of l_{jet} in jetting systems correlates temporally with the onset of deceleration in the expanding particle ring, as quantified by $R_{dense}(t)$, thereby defining the jet initiation time t_{ini}. This section examines the incubation phase preceding jet initiation, with the objective of identifying the governing mechanisms and the influence of structural parameters. A critical focus is on accounting for the absence of jet initiation in certain explosive dispersal systems.

Figures 7(*a*) and 7(*b*) display the r–t diagrams of circumferentially averaged volume fraction ϕ_p and gas pressure P_f, respectively, for a typical jetting system (case 1035-0.6-50-1828). Corresponding results for a non-jetting system (case 1035-0.5-400-1828) are shown in figures 7(*c*) and 7(*d*). Following the sudden release of high-pressure gases from the central cavity, a strong incident shock impinges on the inner surface of the particle ring, generating a radially outward-propagating compaction front (CF). This front delineates the compacted region ($\phi_p = \phi_{comp}$) from the initially uncompacted region ($\phi_p = \phi_0$). Concurrently, a diffusive pressure field develops, driven by the favourable radial pressure gradient ($\nabla_r P_f < 0$) and advances outward, accompanied by progressively intensified gas filtration. The trajectory of the pressure front (PF) can be traced by the flow pressure field in systems where the gaseous velocity becomes non-zero after the arrival of the CF. Conversely, in systems where the gaseous velocity becomes non-zero before the CF arrives, the gaseous velocity field is used for this purpose. Further details are available in our previous work (Miao *et al.* 2024).

https://doi.org/10.1017/jfm.2025.11013 Published online by Cambridge University Press

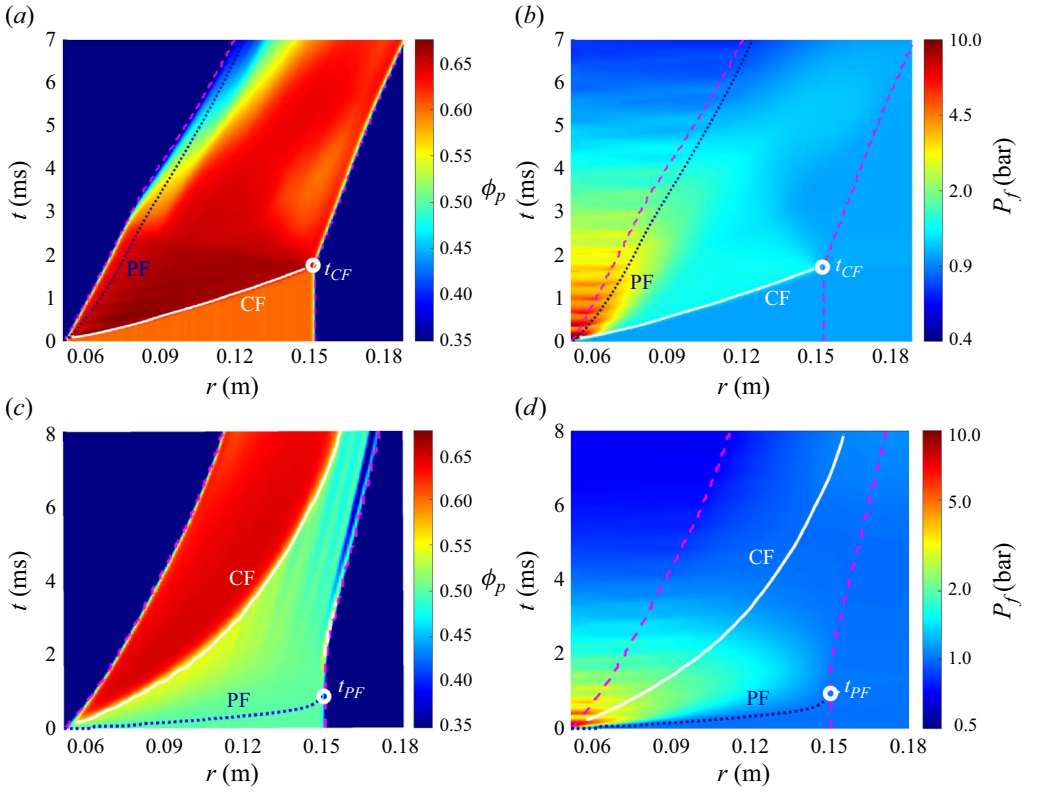


Figure 7. The r–t diagrams of circumferentially averaged volume fraction ϕ_p (a, c) and gas pressure P_f, (b, d) in cases 1035-0.6-50-1828 (a, b) and 1035-0.5-400-1828 (c, d). Trajectories of the CF and PF are overlaid, which intersect with the outer surface of the ring at t_{CF} and t_{PF}.

In case 1035-0.6-50-1828, the PF lags significantly behind the CF. The CF reflects from the ring's outer surface at time t_{CF}, generating an inward-propagating rarefaction wave (RW). In contrast, in case 1035-0.5-400-1828, the PF precedes the CF and reaches the outer surface much earlier. Here, interstitial gas flow behind the PF accelerates particles beyond the CF, resulting in particle velocities exceeding those in the compacted region. Consequently, the CF fails to reach the outer surface, $t_{CF} \sim \infty$, and an outer layer of entirely uncompacted particles detaches from the bulk compacted region (figure 3f). Under these conditions, no RW forms.

Instead of exploring the particle shape effects on force-chain heterogeneity, here, we focus on the mitigating role of gas filtration. When gas filtration dominates, momentum is primarily imparted via interstitial gas flow rather than force chains. Circumferentially uniform gas flows, despite radial flow gradients, produce weaker and spatially sparse force chains, as shown in figure 8(b). The disparity in contact force statistics is evident from the histograms of $\boldsymbol{F}_C$ magnitudes ($|\boldsymbol{F}_C|$) for case 1035-0.6-100-2500 at $t = t_{CF}$ (figure 8c) and case 1035-0.5-400-1828 at $t = t_{PF}$ (figure 8d). Here, $|\boldsymbol{F}_C|$ denotes the magnitude of contact force per unit mass in order to account for amplifying effects arising from increased particle size. Although both distributions of $|\boldsymbol{F}_C|$ exhibit a left skewed unimodal peak spanning $O(10^4)$ to $O(10^6)$ in a log–linear coordinate, the number of effective contacts, n_p, in case 1035-0.6-100-2500 is one order higher than that in case 1035-0.5-400-1828. Specifically, the mean magnitude of $\boldsymbol{F}_C$ per particle, defined as $|\overline{\boldsymbol{F}}_C| = \sum_{i=1}^{N} |\boldsymbol{F}_{C,i}|/N_p$

https://doi.org/10.1017/jfm.2025.11013 Published online by Cambridge University Press

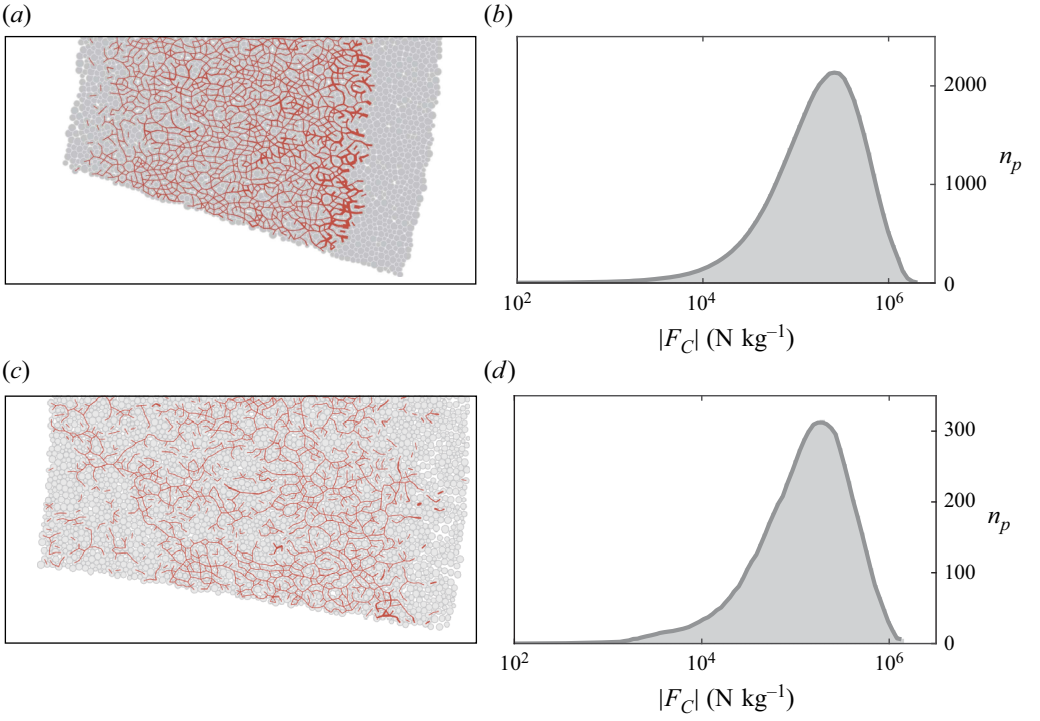


Figure 8. (*a*), (*b*) Networks of force chains comprising inter-particle lines whose thickness scales with the absolute value of normalised contact forces $\hat{F}_C$, $\hat{F}_C = (|F_C| - |F_{C,min}|)/(|F_{C,max}| - |F_{C,min}|)$: (*a*) case 1035-0.6-100-2500, (*b*) case 1035-0.5-400-1828. (*c*), (*d*) Histograms of contact force per unit mass $|F_C|$ for case 1035-0.6-100-2500 at $t = t_{CF}$ (*c*) and case 1035-0.5-400-1828 at $t = t_{PF}$ (*d*).

(where N_p is the total particle number), is $|\overline{\boldsymbol{F}}_C| = 3.5 \times 10^3$ N kg^{-1} for case 1035-0.5-400-1828, two orders of magnitude smaller than that in case 1035-0.6-100-2500 ($|\overline{\boldsymbol{F}}_C| = 1.8 \times 10^5$ N kg^{-1}), manifesting the dominance of gas-mediated momentum transfer over force-chain networks.

The particle velocity fields, $u_p(r,\alpha)$, exhibit spatial heterogeneities inherited from those of the force-chain networks. During the compaction phase in 1035-0.6-100-2500, the contour plot of $u_p(r,\alpha)$ reveals pronounced mesoscale heterogeneity, characterised by localised clusters of particles with exceptionally high velocities (see figure 9*a*). These heterogeneities persist and further amplify during the propagation of RW, evolving into coarser and stronger structures (see figure 9*b*). Ejection of these high-velocity clusters from the outermost layers destabilises the ring's outer surface, forming irregularities which act as jet precursors. In contrast, case 1035-0.5-400-1828 shows no significant circumferential heterogeneities in the $u_p(r,\alpha)$ contour during compaction (see figure 9*c*). A corrugated structure emerges only after full development of gas filtration (figure 9*d*), most likely caused by the burst of localised high-pressure gas pockets generated at loosely packed regions (Sugiyama *et al.* 2019).

The particle velocity fields ($u_p(r, \alpha)$) produce distinct dispersal structures which bear the imprints of their heterogeneity or homogeneity. Figure 10 compares circumferential variations in u_p of jetting particles swept by the RW (figure 10*a*) and the corresponding Voronoi-based packing fraction ($\phi_{p,voro}$) at initiation time (t_{ini}) (figure 10*b*) and at a later stage when jetting patterns are well developed (figure 10*c*). Fluctuations in $u_p(\alpha)$ exhibit strong alignment with $\phi_{p,voro}(\alpha)$ at two instants, with phase correlation coefficients of 0.93

https://doi.org/10.1017/jfm.2025.11013 Published online by Cambridge University Press

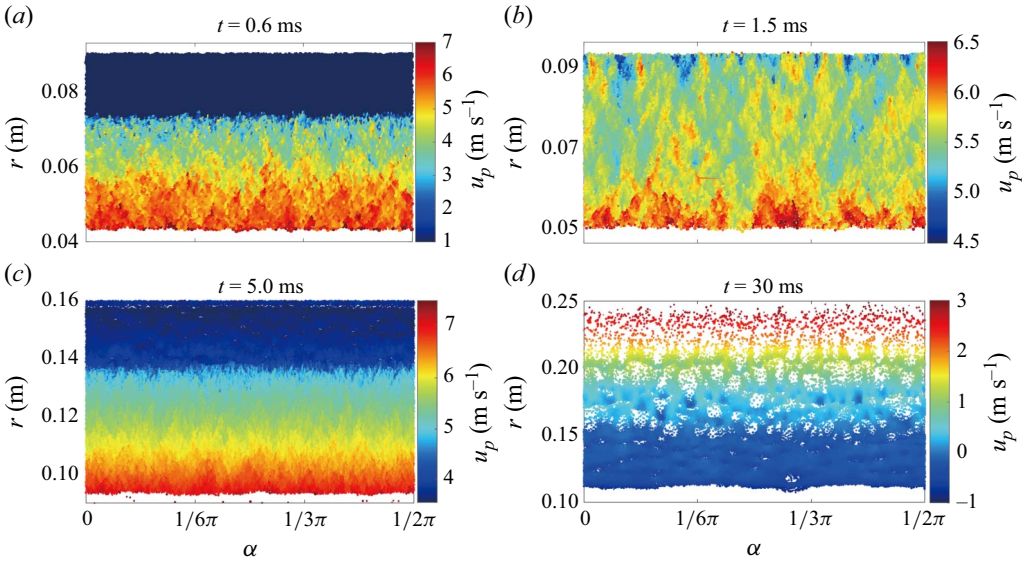


Figure 9. Particle velocity fields, $u_p(r,\alpha)$, in one quarter sector of case 1035-0.6-100-2500 before (*a*) and after (*b*) the refection of the CF from the ring's outer surface, and in 1035-0.5-400-1828 before (*c*) and after (*b*) the full development of gas filtration.

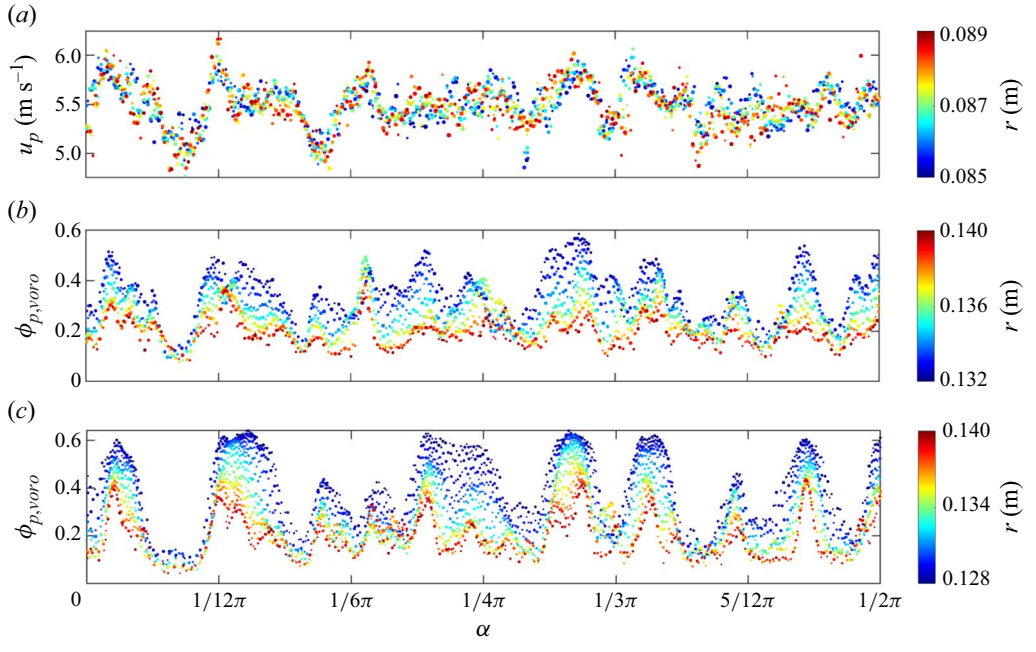


Figure 10. Circumferential variations in u_p of jetting particles swept by the RW (*a*) and the corresponding Voronoi-based packing fraction ($\phi_{p,voro}$) at initiation time (t_{ini}) (*b*) and at a later stage when jetting patterns are well developed (*c*) for case 1035-0.6-100-2500. Scatter points are coloured according to the respective radial coordinates.

https://doi.org/10.1017/jfm.2025.11013 Published online by Cambridge University Press

(at t_{ini}) and 0.92 (at later stages). Hence, these mesoscale velocity field heterogeneities serve as precursors for subsequent jet formation.

Our prior study derived the propagation velocities of the CF (V_{CF}) and PF (V_{PF}) (Sugiyama *et al.* 2019; Miao *et al.* 2024). For densely packed particle layers under steady upstream (P_{UI}) and downstream (P_{DI}) pressures, V_{CF} is governed by

$$V_{CF} = \sqrt{\frac{P_{UI} - P_{DI}}{\rho_p} \frac{\phi_{comp}}{\left(\phi_{comp} - \phi_0\right)\phi_0}}, \tag{3.2}$$

where ϕ_{comp} is the packing fraction in the compacted region. In our simulations, $P_{DI} = P_{amb}$ (ambient pressure), and $P_{UI} = P_f$ (gas pocket pressure). Equation (3.2) indicates that V_{CF} increases with large $\Delta P = P_f - P_{amb}$, lower ρ_p and denser initial packing (larger ϕ_0).

The PF velocity V_{PF} is expressed as

$$V_{PF} = \frac{d_p^2}{150} \frac{(1-\phi_0)^2}{\mu\phi_0^2} \frac{P_f - P_{amb}}{h_{ring}}, \tag{3.3}$$

where μ is the dynamic viscosity of interstitial gases, $h_{ring} = R_{out,0} - R_{in,0}$ is the initial ring thickness. Similar to V_{CF}, V_{PF} increases with larger pressure gradients. Unlike V_{CF}, V_{PF} increases with looser initial packing (smaller ϕ_0), is independent of ρ_p and scales with d_p^2. For the cases 1035-0.6-50-1828 and 1035-0.5-400-1828, P_f, ρ_p and h_{ring} are identical, but d_p is eightfold larger in case 1035-0.5-400-1828, dramatically enhancing V_{PF}. Substituting parameters into (3.2) and (3.3), we calculate V_{CF} and V_{PF} for both cases. For the case 1035-0.6-50-1828, $V_{CF} = 64.8\ \mathrm{m\ s^{-1}}$, exceeds V_{PF} ($V_{PF} = 9.8\ \mathrm{m\ s^{-1}}$). Conversely, for the case 1035-0.5-400-1828, $V_{PF} = 92.6\ \mathrm{m\ s^{-1}}$ surpasses V_{CF} ($V_{CF} = 13\ \mathrm{m\ s^{-1}}$). These theoretical predictions of V_{CF} and V_{PF} as a function of structural parameters successfully resolve the competition between shock compaction and gas filtration observed in the case 1035-0.6-50-1828 (compaction dominated) and 1035-0.5-400-1828 (filtration dominated).

3.4. *Jet growth: macro-scale gas–particle coupling*

During the jet growth phase, initial irregularities at the outer perimeter of the ring, first observed at t_{ini}, evolve into well-defined jets. These jets exhibit substantial longitudinal growth and undergo frequent annihilation and coalescence during the early development phase, as illustrated by the structural evolution of jetting patterns shown in figure 11, where particles are coloured by corresponding Voronoi-based packing fraction $\phi_{p,voro}$ (figure 11*a*), radial component of the particle velocity $u_{p,r}$ (figure 11*b*) and azimuthal component of the particle velocity $u_{p,\alpha}$ (figure 11*c*). Several fine jets coalesce into a coarser one at $t = 12.9$ ms.

The longitudinal growth is driven by the velocity difference between the jet root ($R_{root} \sim R_{dense}$) and the jet tip ($R_{tip} \sim R_{outer}$). Defining V_{root} and V_{tip} as the average particle velocities at all jet roots and tips, respectively, the velocity difference $\Delta V_{jet} = V_{tip} - V_{root}$ governs the elongation dynamics. Figure 12(*a*) illustrates the temporal evolution of V_{root} and V_{tip}, and ΔV_{jet} for the case 1035-0.6-100-2500. Notably, V_{root} decelerates starting at $t = t_{ini}$, eventually reversing direction (becoming negative) due to inward suction forces generated during the ring's implosion. In contrast V_{tip} shows only gradual deceleration after $t = t_{ini}$, remaining positive as it is slowed by drag from surrounding gases.

This divergence in behaviour originates from the spatially non-uniform distribution of the radial pressure gradient $\nabla_r P_f$, as shown in figure 13(*a*). Jet roots, embedded in the dense ring, experience strong adverse pressure gradients ($\nabla_r P_f > 0$) when the internal pressure drops below the ambient external pressure. These gradients counter outward

https://doi.org/10.1017/jfm.2025.11013 Published online by Cambridge University Press

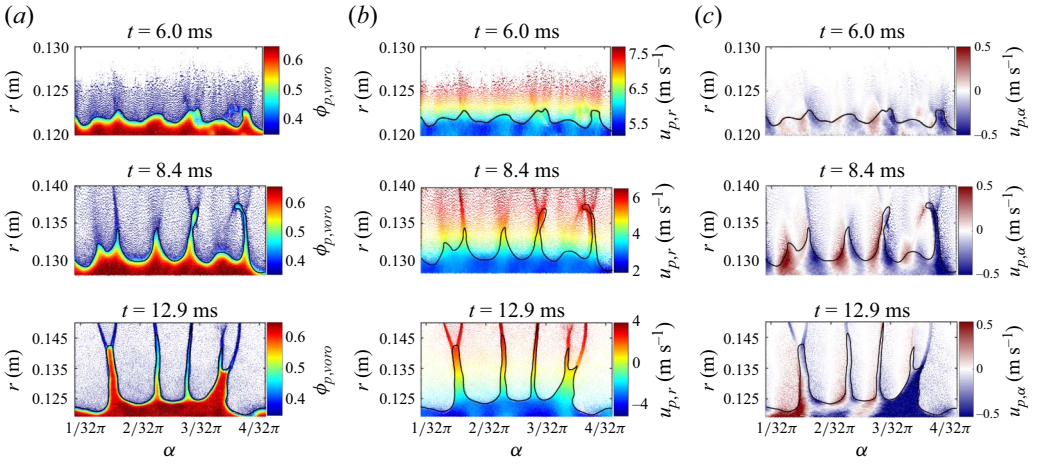


Figure 11. Structural evolution of jetting patterns in one-eighth sector in case 1035-0.6-100-2500 where particles are coloured according to the Voronoi-based packing fraction $\phi_{p,voro}$ (*a*), radial component of particle velocity $u_{p,r}$ (*b*) and azimuthal component of particle velocity $u_{p,\alpha}$ (*c*). The solid curves delineate the jet boundaries and are defined such that particles outside have $\phi_{p,voro} < 0.3$.

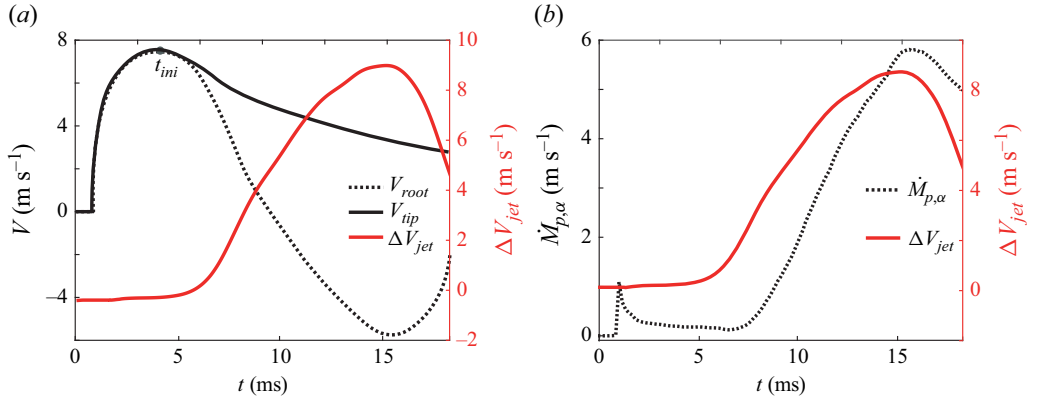


Figure 12. (*a*) Temporal variations in V_{root} and V_{tip}, and ΔV_{jet} for the case 1035-0.6-100-2500. (*b*) Evolutions of cumulative circumferential particle mass flux ($\dot{M}_{p,\alpha}$) and ΔV_{jet} for the case 1035-0.6-100-2500.

motion and drive deceleration of the jet roots. Conversely, the jet tips, characterised by a low packing fraction (figure 11*a*), are exposed to negligible pressure gradients ($\nabla_r P_f \sim 0$), resulting in minimal direct influence from pressure imbalance. Consequently, jet roots are highly sensitive to the time-varying pressure difference during the ring's explosion–implosion cycles, while the outgoing tips remain largely decoupled from the bulk ring dynamics and are instead governed by drag forces from external gases.

Circumferential variations in the radial pressure gradient $\nabla_r P_f$ further modulate ΔV_{jet}. As depicted in figure 13(*a*), ligamental regions (the areas between neighbouring jet roots) exhibit higher $\nabla_r P_f$ due to their thinner layers, driving stronger negative particle radial velocities ($u_{p,r}$) (figure 13*b*) that lead to concave morphologies. This results in an undulating dense ring structure, where thinner ligamental regions interconnect jet roots.

These spatially non-uniform pressure gradients also generate circumferential variations in gas flows. The radial gas velocity ($u_{f,r}$) contours which display two adjacent jets

https://doi.org/10.1017/jfm.2025.11013 Published online by Cambridge University Press

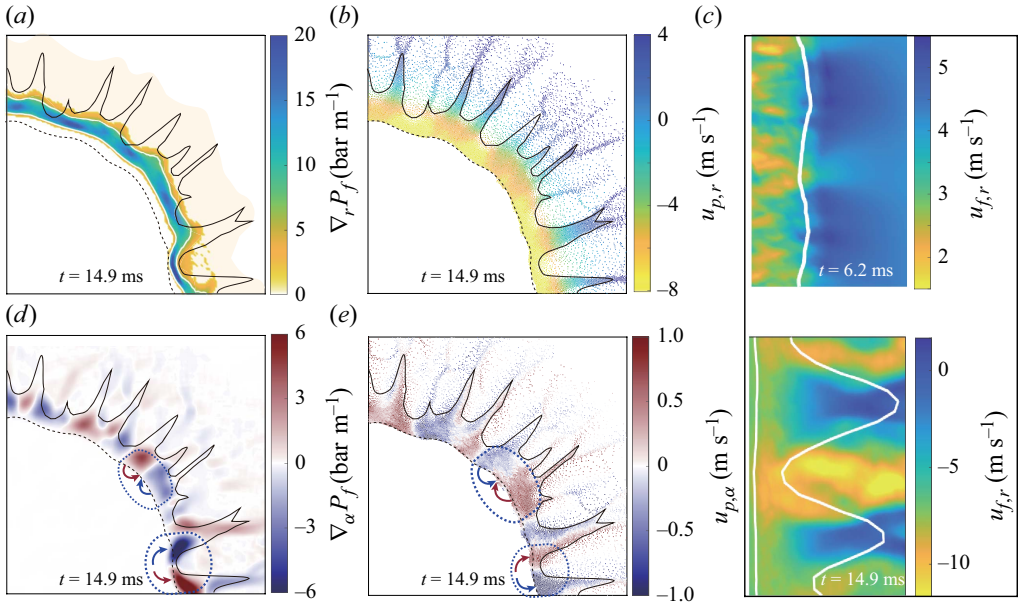


Figure 13. Contours of radial and azimuthal components of gaseous pressure gradients, $\nabla_r P_f$ (*a*) and $\nabla_\alpha P_f$ (*d*), and radial and azimuthal components of particle velocities, $u_{p,r}$ (*b*) and $u_{p,\alpha}$ (*e*). (*c*) Radial gas velocity ($u_{f,r}$) contours spanning two adjacent jets at $t = 6.2$ ms (top) and 14.9 ms (bottom). Solid curves represent the jet boundaries. Dashed boxes in (*d*) and (*e*) indicate strong pressure gradient polarity and the resulting particle vortex formed in the ligament region between two adjacent jets. Dotted boxes in (*d*) and (*e*) indicate pressure gradient polarity and the resulting particle vortex spanning multiple fine jets, which are responsible for the jet coalescence or annihilation.

(figure 13*c*) reveal outward flow ($u_{f,r} > 0$) under favourable pressure gradients until t_{ini}, after which adverse pressure gradients become dominant. Gas flows near ligamental regions decelerate faster and reverse earlier due to intensified adverse $\nabla_r P_f$, while flows through jets persist outward (bottom panel in figure 13*c*), creating spatially dependent drag forces proportional to the local gas–particle velocity differences, $\Delta u_{p\text{-}f} = u_f - u_p$. Particles in ligamental regions hence experience larger inward drag forces than those in jets, further amplifying ΔV_{jet}.

The undulating ring perimeter induces circumferential pressure gradient $\nabla_\alpha P_f$ (figure 13*d*). The opposing $\nabla_\alpha P_f$ polarities flanking coarse jet roots (dashed box in Figure13*d*) drive particles from adjacent ligamental regions toward jets, forming paired particle vortices. These vortices are visualised via the contour of the azimuthal component of particle velocities ($u_{p,\alpha}$) (figure 13*e*). Regions spanning multiple fine jet roots (dotted box in figure 13*d*) exhibit inverted $\nabla_\alpha P_f$ polarities, directing particle migration toward coarser jets and enabling jet coalescence or annihilation.

Post-coalescence, mature jets develop with intensified paired vortices at their roots (figure 11*c*). As ligamental particles are entrained into jet roots, concavity deepens, further enhancing $\nabla_\alpha P_f$ and the particle vortex intensities (figure 11*c*). Vortex intensity, quantified by the circumferential particle mass flux, $\dot{m}_{p,\alpha}$ (defined in Appendix B), has a cumulative value ($\dot{M}_{p,\alpha}$) that correlates with ΔV_{jet}, as shown in figure 12(*b*). Circumferential migration self-sustains until ring implosion halts and favourable pressure gradients resume.

The interplay between ring morphology, pressure gradients and gas flows initiates with the transition from favourable to adverse pressure gradients, triggering ring deceleration

https://doi.org/10.1017/jfm.2025.11013 Published online by Cambridge University Press

and implosion. In systems where rings expand until disintegration (the case 287-0.5-900-4167), adverse pressure gradients negligibly influence the ring, suppressing jet development despite precursor instabilities being abundant. Systems with early ring stagnation (e.g. cases 1035-0.6-400-1828, 1035-0.6-800-1828) exhibit muted jet patterns induced by diminished V_{root} and limited particle migration.

3.5. *Phase diagram of jetting morphology*

Sections 3.3 and 3.4 present the multiscale physics governing the initiation and evolution of explosion-induced particle jets. Jet precursors originate from velocity heterogeneities in shock-compacted particles, mediated by momentum transfer through inter-particle contacts and interstitial gas flows. The mesoscale interplay between particle compaction and gas filtration determines the resultant particle velocity field. Compaction within the granular skeleton generates heterogeneous force-chain networks that drive spatial velocity variations, while interstitial gas flows propagating via diffusive pressure gradients impose homogeneous pressure gradient and drag forces that attenuate velocity fluctuations.

The relative dominance of particle compaction versus gas filtration is quantified by the ratio $\tau_{meso} = t_{CF} / t_{PF}$, where t_{CF} (CF arrival time) and t_{PF} (PF arrival time) characterise the respective time scales for mechanical and gas-dynamic processes to reach the ring's outer surface, respectively. Smaller t_{CF} amplifies localised heterogeneities as discussed in § 3.3, with τ_{meso} in non-jetting systems exceeding jetting systems by several orders of magnitude.

Macroscale jet development, including longitudinal growth, annihilation and coalescence, emerges from the dynamic interaction between the evolving particle ring morphology, localised pressure gradients and gas flows. This mechanism activates only when adverse pressure gradients sufficiently decelerate and implode the ring. To quantify this coupling, we analyse the dense ring's dynamics. The jet tip velocity V_{tip}, approximated by the ring's outer surface expansion velocity V_{out} at t_{ini}, inversely scales with the ring's maximum radius $R_{dense,max}$ (marked with a yellow circle in figure 3*b*). Jet elongation persists over the growth duration Δt_{jet}, proportional to the implosion phase duration Δt_{imp}, itself governed by the implosion amplitude $\Delta\hat{R}_{imp} = (R_{dense,max} - R_{dense,min})/ R_{dense,max}$, where $R_{dense,min}$ is the ring's post-implosion minimum radius, $R_{dense,min} = R_{dense}\ (t_{eva})$. Circumferential particle migration further enhances jetting, with a thicker compacted ring (thickness $h_{ring,comp}$, the distance between R_{dense} and $R_{in,dense}$ when $R_{dense} = R_{dense,max}$, marked with the yellow solid line in figure 3*b*) sustaining stronger particle migration. Integrating these effects, we propose the dimensionless parameter, ξ_{macro}, to characterise macroscale gas-particle coupling intensity

$$\xi_{macro} = \frac{h_{ring,comp}}{R_{dense,max}} \frac{R_{dense,max} - R_{dense,min}}{R_{dense,max}}. \tag{3.4}$$

Continuously expanding rings ($R_{dense,max} = R_{dense,min}$) yield $\Delta\hat{R}_{imp} = 0$ and $\xi_{macro} = 0$, while rings stagnating post-implosion ($R_{dense,min} \sim R_{dense,max}$) exhibit low ξ_{macro}. Calculated ξ_{macro} for cases 1035-0.6-50-1828, 1035-0.6-100-2500, 1035-0.6-400-1828, 1035-0.6-800-1828, 287-0.5-900-4167 and 1014-0.5-400-1828, are 1.1×10^{-1}, 5.8×10^{-2}, 7.9×10^{-4}, 8.1×10^{-4}, 0, 7.0×10^{-4}, respectively.

Figure 14 maps all numerical cases in the τ_{meso}–ξ_{macro} parameter space with symbols colour coded according to their ω_{jet} values. Systems with $\tau_{meso} \geq O(10^1)$ or $\xi_{macro} \leq O(10^{-3})$ exhibit negligible ω_{jet}, classified as non-jetting due to absent precursors or insufficient driving forces. Beyond this regime, ω_{jet} increases with decreasing τ_{meso} and/or increasing ξ_{macro}, peaking at $\omega_{jet} \sim O(10^1)$, in regions where $\tau_{meso} \sim O(10^{-1})$ and ξ_{macro}

https://doi.org/10.1017/jfm.2025.11013 Published online by Cambridge University Press

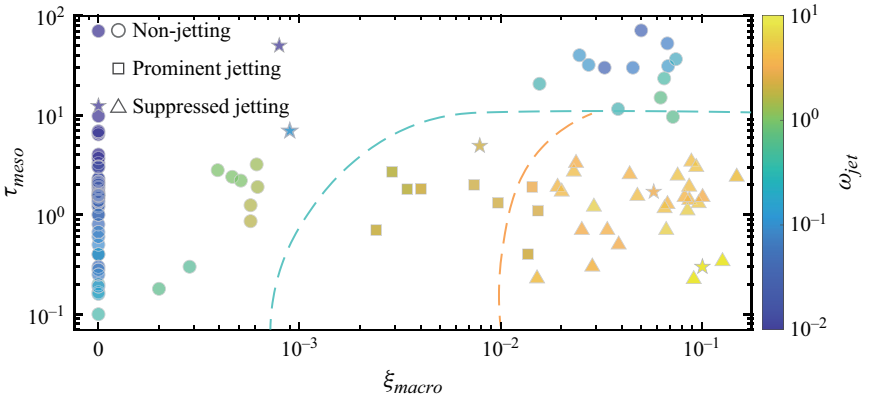


Figure 14. Distribution of all numerical cases in the τ_{meso}–ξ_{macro} parameter space with symbols colour coded according to their ω_{jet} values. Star symbols denote numerical cases from figures 3 and 4, from top left to bottom right: 1014-0.5-400-1828, 287-0.5-900-4167, 1035-0.6-800-1828, 1035-0.6-400-1828, 1035-0.6-100-2500, 1035-0.6-50–1828.

$\sim O(10^{-1})$, corresponding to prominent jetting structures. Intermediate systems exhibit suppressed jetting with ω_{jet} rising gradually towards the jetting regime. Star symbols denote numerical cases from figures 2 and 3.

This phase diagram consolidates macro- and microscale properties, including the M/C, explosion energy (P_f), geometric parameters (R_{gas}, $R_{in,0}$, $R_{out,0}$), initial packing fraction (ϕ_0), particle density (ρ_p) and size (d_p), into the dimensionless parameters τ_{meso} and ξ_{macro}, which encapsulate the multiscale physics of jet formation. Angular particles, however, introduce additional complexities to the jetting phase diagram. Force-chain networks in angular particle packings exhibit greater heterogeneity due to interlocking and friction (Seo *et al.* 2024), yielding coarser jet structures. Compaction dynamics and gas filtration also diverge from spherical systems, with potential contributions from particle fracture, asperity attrition and plastic deformation. Existing parameters τ_{meso} and ξ_{macro} inadequately account for these effects, necessitating further exploration of microscale processes to refine the jetting phase diagram.

4. Discussion

As elaborated in § 3.5, the jetting morphology is governed by two dimensionless parameters, τ_{meso} and ξ_{macro}, which characterise the multiscale physics of jet initiation and growth, respectively. A primary challenge in utilising τ_{meso} and ξ_{macro} arises from their derivation, which requires comprehensive knowledge of coupled particle–gas dynamics spanning meso-, and macro-scales. Such dynamics is typically resolved via computationally intensive multiphase flow simulations, which treat granular phases as continuum/discrete media with resolved/unresolved particles and advanced coupling models (Sundaresan, Ozel & Kolehmainen 2018; Zhao, Zhao & Luding 2023). For 3-D explosive dispersal systems involving millions (or even billions) of particles, these simulations become prohibitively expensive.

To address this, we adopted a continuum-based explosive dispersal model, previously developed to integrate meso- and macro-scale gas–particle couplings (Miao *et al.* 2024) and updated with an advanced filtration model. This model reproduces critical processes such as shock-induced particle compaction, gas filtration and ring pulsation, enabling

https://doi.org/10.1017/jfm.2025.11013 Published online by Cambridge University Press

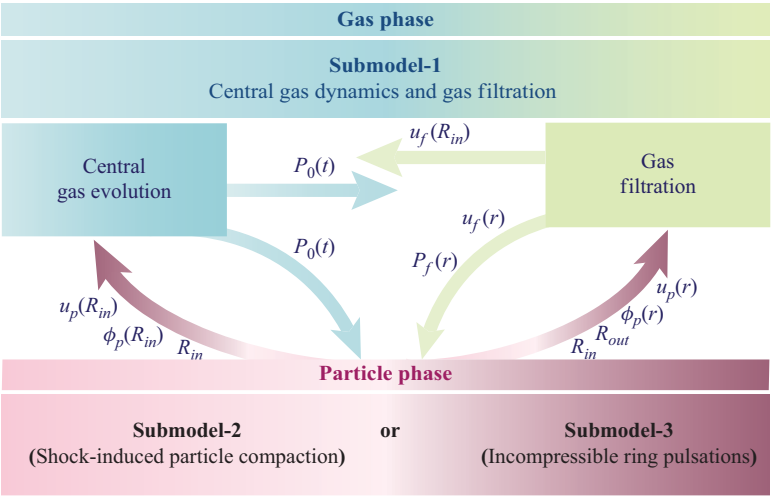


Figure 15. Workflow diagram of the explosive dispersal model, illustrating iterative information exchange between submodels.

theoretical prediction of τ_{meso} and ξ_{macro} at modest computational cost. Consequently, the jetting regime for an arbitrary system can be properly determined.

The explosive dispersal model comprises three interconnected submodels: (i) submodel-1 governs the central gas dynamics and gas filtration through the granular medium; (ii) submodel-2 accounts for the shock-induced particle compaction driven by the diffusional pressure gradients and interphase drag forces; (iii) submodel-3 calculates pulsations of the incompressible compacted particle ring. Within this framework, particle rings are treated as porous media, with the propagation of the CF modelled via the momentum balance equation and jump conditions across the CF. Gases in the central pocket undergo adiabatic evolution, bounded by an expanding or imploding ring, while sustaining persistent gas filtration. The terminal state of submodel-2 (post-shock compaction) provides the initial conditions for submodel-3.

Figure 16 presents the workflow diagram of the explosive dispersal model, illustrating iterative data exchange between submodels. Compared with the original model (Miao *et al.* 2024), key modifications include a mixed-flow equation governing gas filtration, which incorporates inertial and viscous effects critical for high-speed flows (see Appendices III for governing equations). The model assumes circumferential uniformity in shock-compaction velocity fields, employing 1-D polar coordinates with radial distance as the sole spatial variable. Rarefaction effects, particle ejection and diffusion, as well as bulk breakaway, are neglected, and we focus instead on the densely packed particle ring bounded by radii of $R_{in,dense}$ and R_{dense}.

Validation against numerical simulations (figure 16) reveals strong agreement for cases with intact particle rings (1035-0.6-50-1828, 1035-0.6-400-1828), where theoretical trajectories of inner/outer ring radii ($R_{in}^{the}(t)$ and $R_{out}^{the}(t)$) and compaction/pressure fronts ($R_{CF}^{the}(t)$ and $R_{PF}^{the}(t)$) agree well with numerical counterparts ($R_{in}^{num}(t)$, $R_{dense}^{num}(t)$, $R_{CF}^{num}(t)$ and $R_{PF}^{num}(t)$). For the case 287-0.5-900-4167 involving a quite thin particle ring ($h_{ring,\mathrm{comp}} = 44\ d_\mathrm{p}$) under high gas pressure, the model captures shock compaction and gas filtration but fails to predict ring disintegration, instead yielding unphysical high-amplitude pulsations. This discrepancy arises from the momentum-dominated dynamics in thin rings ($h_{ring,comp}/R_{imp} \to 0$), causing $\xi_{macro} \to 0$, consistent with observed trend in ξ_{macro} in systems exhibiting persistent expansion prior to disintegration.

https://doi.org/10.1017/jfm.2025.11013 Published online by Cambridge University Press

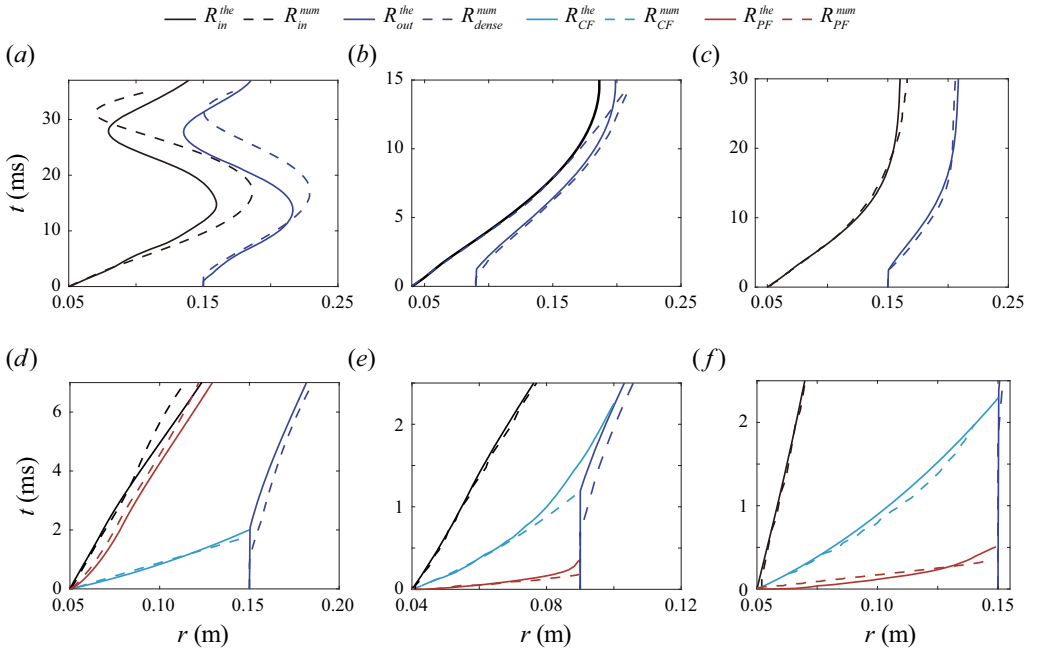


Figure 16. Comparisons of predicted and simulated trajectories of inner/outer ring radii (*ac*), $R_{in}^{the}(t)$ and $R_{out}^{the}(t)$ vs $R_{in}^{num}(t)$, $R_{dense}^{num}(t)$, and compaction/pressure fronts (*df*), $R_{CF}^{the}(t)$ and $R_{PF}^{the}(t)$ vs $R_{CF}^{num}(t)$ and $R_{PF}^{num}(t)$. Panels (*a*) and (*d*) show case 1035-0.6-50-1828, (*c*) and (*e*) show case 287-0.5-900-4167 and (*d*) and (*f*) show case 1035-0.6-400-1828.

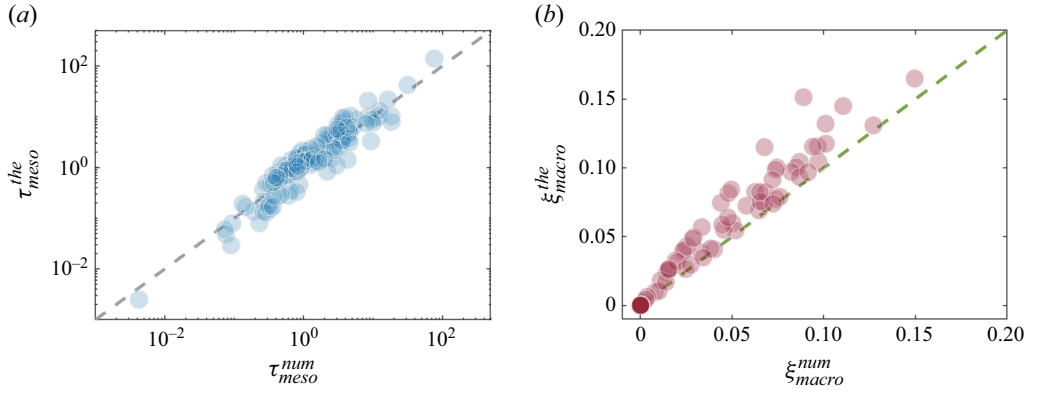


Figure 17. Comparisons of predicted and simulated τ_{meso} (*a*), τ_{meso}^{the} vs τ_{meso}^{num}, and x_{macro} (*b*), ξ_{macro}^{the} vs ξ_{macro}^{num}. The coefficients of determination are 0.92 and 0.97, respectively.

Theoretical and numerical predictions of τ_{meso} and ξ_{macro} show strong consistencies (figures 17*a* and 17*b*), enabling construction of a jetting phase diagram within the τ_{meso}–ξ_{macro} parameter space. It is crucial to emphasise that this predictive framework is predicated on, and strictly applicable to, the weak-shock regime driven by pressurised gas expansion. This diagram provides a robust predictive framework for jetting morphologies under these specific conditions, integrating multiscale gas–particle couplings. However, the 1-D formulation neglects discrete particle effects, e.g. clustering, breakaway and 3-D phenomena, such as axial gas leakage and traverse particle migration. Experimental

https://doi.org/10.1017/jfm.2025.11013 Published online by Cambridge University Press

observations suggest angular particles amplify jet coarseness, which is most likely associated with enhanced heterogeneous force-chain networks (Seo *et al.* 2024). Hence, stochastic descriptors of shape and contact mechanics need to be taken into account to enhance fidelity to real granular systems. Future refinements must incorporate 3-D flow physics and validate against large-scale experiments with diverse geometries and confinement conditions, particularly for applications requiring jetting pattern control, such as blast mitigation or fuel–air mixing efficiency.

5. Conclusions

This study elucidates the multiscale physics governing explosion-induced particle jetting in the weak-shock regime through an integrated numerical, and theoretical approach. Our findings reveal that jet precursors emerge from the interplay between mesoscale gas filtration and microscale heterogeneities of force-chain networks formed during shock compaction. Subsequent macroscale ring implosion, driven by adverse pressure gradients, amplifies initial perturbations into coherent jet structures. By unifying the physics of jet initiation and growth, we consolidate the influence of micro- and macroscale parameters into two dimensionless quantities: τ_{meso}, governing precursor formation, and ξ_{macro}, dictating jet amplification. A phase diagram for gas-driven systems constructed in the τ_{meso}–ξ_{macro} space categorises jetting morphologies into three distinct regimes, namely non-jetting, suppressed jetting and prominent jetting. Finally, we propose a modified continuum-based explosive dispersal model that reproduces the critical dynamics while serving as a computationally efficient framework for jetting regime prediction.

Funding. This work was supported by the following funding sources:

(i) The National Natural Science Foundation of China (Joint Fund Project, Grant No. U2341243).
(ii) The State Key Laboratory of Explosion Science and Technology (Grant No. ZDKT23-01).
(iii) The Open Research Project of the National Key Laboratory of Computational Physics, Beijing Institute of Applied Physics and Computational Mathematics (Grant No. JK2024-06).

Declaration of interests. The authors report no conflicts of interest.

Appendix A. Numerical case parameters, parameter analysis and early-time dynamics

A.1. *Details of parameters in each numerical case*

Case number	M/C	P_0 (bar)	R_{gas} (mm)	$R_{in,0}$ (mm)	$R_{out,0}$ (mm)	ϕ_0	ρ_p (kg m^{-3})	d_p (μm)	ω_{jet}
1	1035	20	60	80	180	0.6	5625	400	0.003
2	1035	20	40	60	160	0.6	2955	400	0.007
3	266	108	20	40	90	0.5	4167	300	0.007
4	4139	5	30	50	150	0.6	1828	400	0.009
5	2875	10	20	40	90	0.5	4167	900	0.010
6	60	9.7	40	40	50	0.5	2500	100	0.01100
7	2264	10	30	50	150	0.6	2000	200	0.01300
8	9.700	443	20	40	57	0.5	2500	100	0.01300
9	1014	17	30	50	150	0.5	1828	400	0.01500
10	266	108	20	40	90	0.5	4167	100	0.01500

Table 1. For caption see next page.

https://doi.org/10.1017/jfm.2025.11013 Published online by Cambridge University Press

Case number	M/C	P_0 (bar)	R_{gas} (mm)	$R_{in,0}$ (mm)	$R_{out,0}$ (mm)	ϕ_0	ρ_p (kg m^{-3})	d_p (μm)	ω_{jet}
11	287	100	20	40	90	0.5	4167	900	0.01500
12	1014	17	60	80	180	0.5	5625	400	0.01600
13	266	71.30	20	40	70	0.65	4167	900	0.01600
14	48	183	60	80	140	0.5	5625	600	0.01600
15	27	198	20	40	57	0.6	2500	100	0.01600
16	48	183	30	50	110	0.5	1934	600	0.01900
17	1051	10	40	60	160	0.6	1500	400	0.0200
18	5	336	20	40	46	0.6	2500	100	0.0200
19	1150	25	20	40	90	0.5	4167	500	0.02200
20	3002	7	40	60	160	0.6	3000	400	0.02300
21	104	100	20	40	90	0.5	1503	100	0.02400
22	9	443	20	40	54	0.6	2500	100	0.02500
23	137	200	20	40	70	0.65	6000	900	0.02600
24	172	100	20	40	90	0.5	2500	100	0.02600
25	48	183	30	50	110	0.5	1934	200	0.02600
26	159	55	20	40	70	0.5	2500	100	0.02800
27	55	183	40	60	120	0.5	3506	600	0.02900
28	55	220	40	60	120	0.6	3506	600	0.02900
29	9.700	245	20	40	50	0.5	2500	100	0.03200
30	192	90	20	40	90	0.5	2500	100	0.03200
31	283	20	30	50	150	0.6	500	600	0.03300
32	48	183	60	80	140	0.5	5625	200	0.03400
33	55	220	40	60	120	0.6	3506	200	0.03400
34	97	108	20	40	70	0.6	2500	100	0.03600
35	287	78	20	40	90	0.65	2500	100	0.03700
36	374	60	20	40	90	0.65	2500	412	0.03700
37	18	17	60	80	180	0.5	100	400	0.03900
38	48	183	20	40	70	0.5	2500	100	0.03900
39	55	183	40	60	120	0.5	3506	200	0.04100
40	191	55	20	40	70	0.6	2500	100	0.04400
41	48	220	30	50	110	0.6	1934	600	0.04500
42	155	180	20	40	110	0.5	2500	100	0.05000
43	1015	17	40	60	160	0.5	2955	400	0.05200
44	2875	10	20	40	90	0.5	4167	62	0.05200
45	26	91	20	40	50	0.5	2500	100	0.06100
46	48	220	60	80	140	0.6	5625	600	0.06200
47	26	336	20	40	70	0.5	2500	100	0.06200
48	27	165	20	40	57	0.5	2500	100	0.07400
49	241	78	20	40	90	0.65	2100	216	0.08200
50	862	20	20	40	90	0.5	2500	300	0.08800
51	5161	8	20	40	131	0.5	2500	100	0.09100
52	207	100	20	40	90	0.6	2500	100	0.09700
53	224	100	20	40	90	0.65	2500	100	0.1110
54	53	100	20	40	57	0.6	2500	100	0.1180
55	552	20	60	80	180	0.6	3000	200	0.1200
56	2875	10	20	40	90	0.5	4167	90	0.1490
57	690	10	20	40	90	0.5	1000	180	0.1490
58	48	220	30	50	110	0.6	1934	200	0.1590
59	852	30	20	40	106	0.5	2500	100	0.1600
60	490	200	20	40	180	0.6	2500	100	0.1740
61	48	220	60	80	140	0.6	5625	200	0.2100

Table 1. For caption see next page.

https://doi.org/10.1017/jfm.2025.11013 Published online by Cambridge University Press

Case number	M/C	P_0 (bar)	R_{gas} (mm)	$R_{in,0}$ (mm)	$R_{out,0}$ (mm)	ϕ_0	ρ_p (kg m^{-3})	d_p (μm)	ω_{jet}
62	6973	4.400	20	40	106	0.5	2500	100	0.2100
63	1035	20	40	60	160	0.6	2955	50	0.2160
64	1023	25	20	40	106	0.5	2500	100	0.2180
65	103	200	20	40	90	0.6	2500	100	0.2270
66	241	78	20	40	90	0.65	2100	342	0.2300
67	1035	20	30	50	150	0.6	1828	800	0.2400
68	6898	3	20	40	90	0.6	2500	100	0.2500
69	287	70	20	40	90	0.65	2500	100	0.2510
70	1014	17	20	40	90	0.5	2500	100	0.2890
71	876	10	20	40	70	0.5	2500	100	0.2990
72	2875	10	20	40	90	0.5	4167	180	0.3300
73	9198	36	20	40	90	0.5	48000	60	0.3400
74	2276	5	20	40	70	0.65	2500	100	0.3400
75	374	60	20	40	90	0.65	2500	50	0.3500
76	4776	7	20	40	110	0.6	2500	100	0.3680
77	345	60	20	40	90	0.6	2500	630	0.4100
78	6920	6	20	40	121	0.6	2500	100	0.4200
79	1035	20	30	50	150	0.6	1828	600	0.4300
80	207	55	20	40	70	0.65	2500	100	0.4600
81	241	78	20	40	90	0.65	2100	58	0.4700
82	241	78	20	40	90	0.65	2100	80	0.4770
83	48	220	20	40	70	0.6	2500	100	0.5130
84	4765	7.6	20	40	110	0.65	2500	100	0.5680
85	374	60	20	40	90	0.65	2500	192	0.5730
86	862	20	20	40	90	0.5	2500	100	0.6
87	287	97	20	40	110	0.5	2500	100	0.9810
88	58	50	20	40	90	0.5	417	900	0.9810
89	207	60	20	40	90	0.6	1500	630	0.9810
90	479	60	20	40	90	0.5	4167	100	1.210
91	173	60	20	40	90	0.5	2500	100	1.444
92	287	55	20	40	90	0.550	2500	100	1.611
93	345	60	20	40	90	0.6	2500	100	1.704
94	287	60	20	40	90	0.5	1503	100	1.720
95	287	60	40	60	172	0.5	2500	100	1.788
96	2060	17	40	60	160	0.5	6000	50	1.830
97	2060	17	40	60	160	0.5	6000	40	1.940
98	5964	9	20	40	131	0.65	2500	100	1.970
99	310	108	20	40	110	0.6	2500	100	2.005
100	1035	20	30	50	150	0.6	1828	400	2.014
101	102	20	30	50	150	0.6	180	600	2.116
102	5190	8	20	40	121	0.6	2500	100	2.116
103	5170	8.7	20	40	121	0.65	2500	100	2.149
104	24	20	30	50	150	0.5	50	600	2.183
105	288	36	20	40	90	0.5	1503	60	2.268
106	345	60	20	40	90	0.6	2500	400	2.390
107	575	50	20	40	90	0.5	4167	900	2.900
108	1014	17	60	80	180	0.5	5625	50	2.924
109	575	50	20	40	90	0.5	4167	560	3.100
110	4410	21.60	20	81	171	0.65	2500	100	3.165
111	632	78	20	40	90	0.65	5500	216	3.240

Table 1. For caption see next page.

https://doi.org/10.1017/jfm.2025.11013 Published online by Cambridge University Press

Case number	M/C	P_0 (bar)	R_{gas} (mm)	$R_{in,0}$ (mm)	$R_{out,0}$ (mm)	ϕ_0	ρ_p (kg m^{-3})	d_p (μm)	ω_{jet}
112	2076	20	20	40	121	0.6	2500	100	3.243
113	1035	20	60	80	180	0.6	5625	50	3.276
114	288	36	20	40	90	0.5	1503	120	3.325
115	599	145	20	40	170	0.6	2500	100	3.460
116	1014	17	30	50	150	0.5	1828	50	3.540
117	796	26	20	40	90	0.6	2500	100	3.651
118	692	50	20	40	121	0.5	2500	100	3.808
119	1035	20	20	40	90	0.6	2500	100	3.988
120	1035	9	30	40	90	0.6	2500	100	3.900
121	697	44	20	40	106	0.6	2500	100	3.923
122	649	145	20	40	170	0.65	2500	100	3.961
123	1534	20	20	40	106	0.6	2500	100	3.786
124	1014	17	60	80	180	0.5	5625	100	4.140
125	288	36	20	40	90	0.5	1503	80	4.155
126	500	145	20	40	170	0.5	2500	100	4.405
127	1015	17	40	60	160	0.5	2955	50	4.434
128	688	60	20	40	131	0.5	2500	100	4.501
129	690	30	20	40	90	0.6	2500	100	4.506
130	288	36	20	40	90	0.5	1503	100	4.534
131	805	108	20	40	170	0.6	2500	100	4.547
132	492	52	20	40	106	0.5	2500	100	4.600
133	58	25	20	40	90	0.5	210	500	4.763
134	1023	30	20	40	106	0.6	2500	100	4.811
135	4903	20	20	40	180	0.6	2500	100	4.885
136	2069	10	20	40	90	0.6	2500	100	4.972
137	1538	27	20	40	121	0.6	2500	100	5.211
138	1038	40	20	40	121	0.6	2500	100	5.921
139	451	108	20	40	130	0.6	2500	100	6.059
140	692	60	20	40	121	0.6	2500	100	6.171
141	2012	18	20	40	110	0.65	2500	100	7.123
142	2043	48	20	40	180	0.6	2500	100	7.223
143	1035	20	30	50	150	0.6	1828	50	8.797

Table 1. Parameters in numerical cases.

A.2. *Comparative analysis of single parameter*

Table 1 presents the detailed parameters for each numerical case shown in figures 2(*b*) and 2(*c*), including the initial pressure and radius of the central gas pocket (P_0, R_{gas}), the initial inner radius, outer radius and packing fraction of the particle ring ($R_{in,0}$, $R_{out,0}$, f_0), as well as the particle diameter and density (d_p, ρ_p). The combined effects of these parameters are illustrated in figures 3 and 4 and discussed in detail. To investigate the influence of individual parameters, this appendix conducts a comparative analysis by varying only one parameter while keeping the others constant.

Figure 18 shows the jetting morphologies in five cases where only P_0 is varied, while all other parameters remain the same ($R_{gas} = 20$ mm, $R_{in,0} = 40$ mm, $R_{out,0} = 90$ mm, $\phi_0 = 0.6$, $d_p = 100$ μm, $\rho_p = 2500$ kg m^{-3}). From figures 18(*a*) to 18(*d*), as P_0 decreases from 60 to 20 bar, the number of finger-like protrusions remains nearly constant at approximately 9. However, as P_0 decreases, the mass ratio (M/C) increases from 692 to 2076, nearly tripling, resulting in less energy being imparted per unit mass of particles. As a result, a large portion of particles remains densely packed, and only a minimal fraction disperses outward. Consequently, lower $\phi_{jetting}$ leads to a decrease in the jetting intensity indicator ω_{jet} from 6.17 to 3.24. When P_0 is further reduced to 8 bar

https://doi.org/10.1017/jfm.2025.11013 Published online by Cambridge University Press

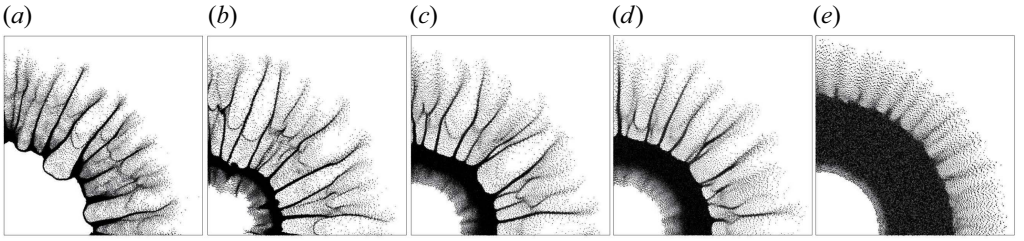


Figure 18. Contours of jetting morphologies in case 140 ($P_0 = 60$ bar, $M/C = 692$) (*a*), case 138 ($P_0 = 40$ bar, $M/C = 1038$) (*b*), case 137 ($P_0 = 27$ bar, $M/C = 1538$) (*c*), case 112 ($P_0 = 20$ bar, $M/C = 2076$) (*d*), case 102 ($P_0 = 8$ bar, $M/C = 5190$) (*e*). Other parameters in (*a*)–(*e*) remain constant: $R_{gas} = 20$ mm, $R_{in,0} = 40$ mm, $R_{out,0} = 90$ mm, $\phi_0 = 0.6$, $d_p = 100\,\mu$m, $\rho_p = 2500$ kg m^{-3}.

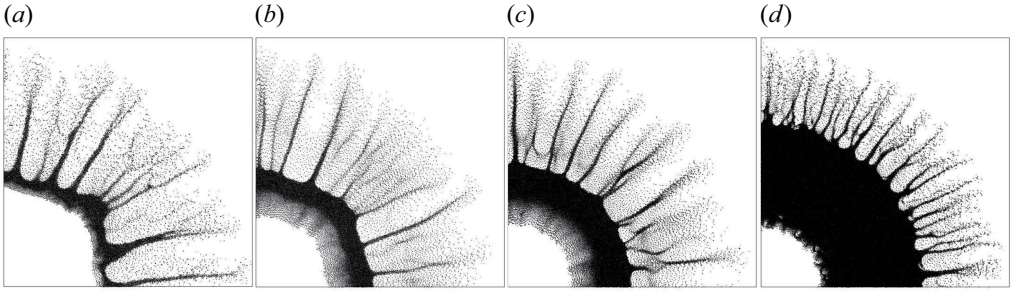


Figure 19. Contours of jetting morphologies in case 119 ($R_{out,0} = 90$ mm, $M/C = 1035$) (*a*), case 123 ($R_{out,0} = 106$ mm, $M/C = 1534$) (*b*), case 112 ($R_{out,0} = 121$ mm, $M/C = 2076$) (*c*), case 135 ($R_{out,0} = 180$ mm, $M/C = 4903$) (*d*). Other parameters in (*a*)–(*d*) remain constant: $P_0 = 20$ bar, $R_{gas} = 20$ mm, $R_{in,0} = 40$ mm, $\phi_0 = 0.6$, $d_p = 100\,\mu$m, $\rho_p = 2500$ kg m^{-3}.

(figure 18*e*), M/C increases to 5190, and the energy delivered to the particle ring becomes insufficient to drive significant ring expansion. Consequently, the amplitude of ring contraction is also significantly reduced, resulting in a very low macroscopic implosion intensity parameter ξ_{macro}. Under these conditions, the initial protrusions neither merge nor elongate substantially, ultimately forming a larger number (14) of finer and shorter protrusions, characterised by a low jetting intensity ($\omega_{jet} = 2.11$).

Similar to the influence of decreasing P_0, increasing $R_{out,0}$ seems to contribute to thicker protrusions. Figure 19 shows the jetting morphologies in four cases where only $R_{out,0}$ is varied, while all other parameters remain the same ($P_0 = 20$ bar, $R_{gas} = 20$ mm, $R_{in,0} = 40$ mm, $\phi_0 = 0.6$, $d_p = 100\,\mu$m, $\rho_p = 2500$ kg m^{-3}). Similarly, as $R_{out,0}$ increases from 90 to 121 mm (figures 19*a* to 19*c*), the mass ratio (M/C) increases from 1035 to 2076, nearly doubling. Consequently, there is an increasing portion of particles staying in the densely packed region and fewer particles forming the particle jet in the jetting region. The number of finger-like protrusions increased marginally, from 9 to 10. As a result, ω_{jet} decreased slightly from 3.99 to 3.79 (figure 19*a–c*). However, as $R_{out,0}$ further increases form 121 to 180 mm (figure 19*c–d*), the mass ratio (M/C) increases from 2076 to 4903, in addition to the increasing thicker densely packed region, the number of finger-like protrusions also almost doubles, from 10 to 21. This dramatic change possibly can be attributed to the larger circumference at the particle ring's outer interface ($2\pi\ R_{out,0}$), which provides the physical space for more potential jet 'seeds' to exist.

As shown in figures 18 and 19, P_0 and $R_{out,0}$ are more likely to alter the thickness, length and number of radial protrusions by influencing the development of jetting seeds

https://doi.org/10.1017/jfm.2025.11013 Published online by Cambridge University Press

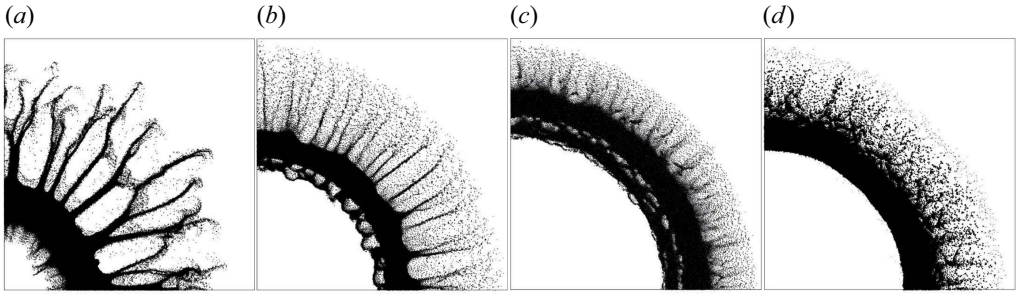


Figure 20. Contours of jetting morphologies in case 143 ($d_p = 50\,\mu$m, $M/C = 1035$) (a), case 100 ($d_p = 400\,\mu$m, $M/C = 1035$) (b), case 79 ($d_p = 600\,\mu$m, $M/C = 1035$) (c), case 67 ($d_p = 800\,\mu$m, $M/C = 1035$) (d). Other parameters in (a)–(d) remain constant: $P_0 = 20$ bar, $R_{gas} = 30$ mm, $R_{in,0} = 50$ mm, $R_{out,0} = 150$ mm, $\phi_0 = 0.6$, $\rho_p = 1828\,\mathrm{kg\,m^{-3}}$.

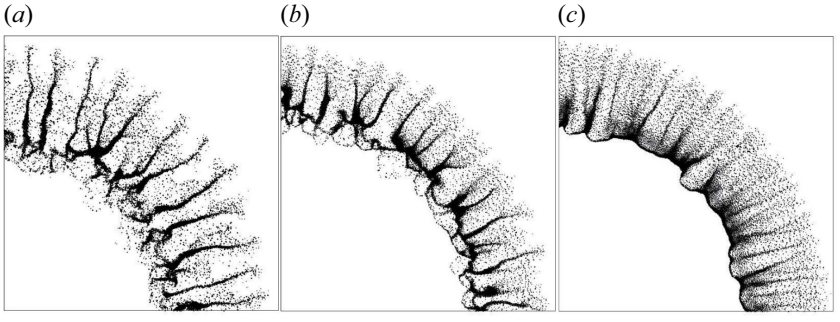


Figure 21. Contours of jetting morphologies in case 94 (173-60-0.5-50-100-1503) (a), case 91 (287-60-0.5-50-100-2500) (b), case 90 (479-60-0.5-50-100-4167) (c).

development. However, prior to that, the jetting seeds is determined by particle properties, such as particle diameter and density. Figure 20 shows the jetting morphologies in four cases where only d_p is varied, while all other parameters keep constant ($P_0 = 20$ bar, $R_{gas} = 20$ mm, $R_{in,0} = 40$ mm, $R_{out,0} = 150$ mm, $\phi_0 = 0.6$, $\rho_p = 2500\,\mathrm{kg\,m^{-3}}$).With d_p increasing from 50 μm to 400 μm (figures 20*a* to 20*b*), jetting morphologies change from thick finger-like protrusions (figure 20*a*) to a filamentary pattern (figure 20*b*). When d_p further increases to 600 μm (figure 20*c*) and 800 μm (figure 20*d*), particle jetting is further weakened, the filamentary structure is replaced by diffuse layers (figure 20*c–d*). The value of ω_{jet} for cases shown in figure 20(*a–d*) is 8.8, 2.01, 0.43 and 0.24, respectively.

Figure 21 shows the transition of jetting morphologies with ρ_p. Cases shown in figure 21(*a*)–(*c*) hold ρ_p at 1503 kg m^{-3}, 2500 kg m^{-3}, 4167 kg m^{-3}, respectively, with other parameters kept the same ($P_0 = 60$ bar, $R_{gas} = 20$ mm, $R_{in,0} = 40$ mm, $R_{out,0} = 90$ mm, $\phi_0 = 0.5$, $d_p = 100\,\mathrm{kg\,m^{-3}}$). As shown in figure 21, the jetting morphologies are less sensitive to ρ_p compared with d_p; with ρ_p increasing from 1503 to 2500, then to 4167 (figure 21*a–c*), the jetting structure gets slimer, represented by the decrease of ω_{jet} from 1.61 to 1.44 then to 1.21.

It is noted that the above discussion is only valid under corresponding circumstances, as jetting morphologies are determined by the combined effects of all parameters. For example, a lower P_0 for cases with relatively small $M/C \sim O(10^1)$ might increase the amplitude of ring contraction by suppressing the fast expansion and collapsing of the particle ring. In such a situation, lower P_0 will contribute to more prominent particle jetting

https://doi.org/10.1017/jfm.2025.11013 Published online by Cambridge University Press

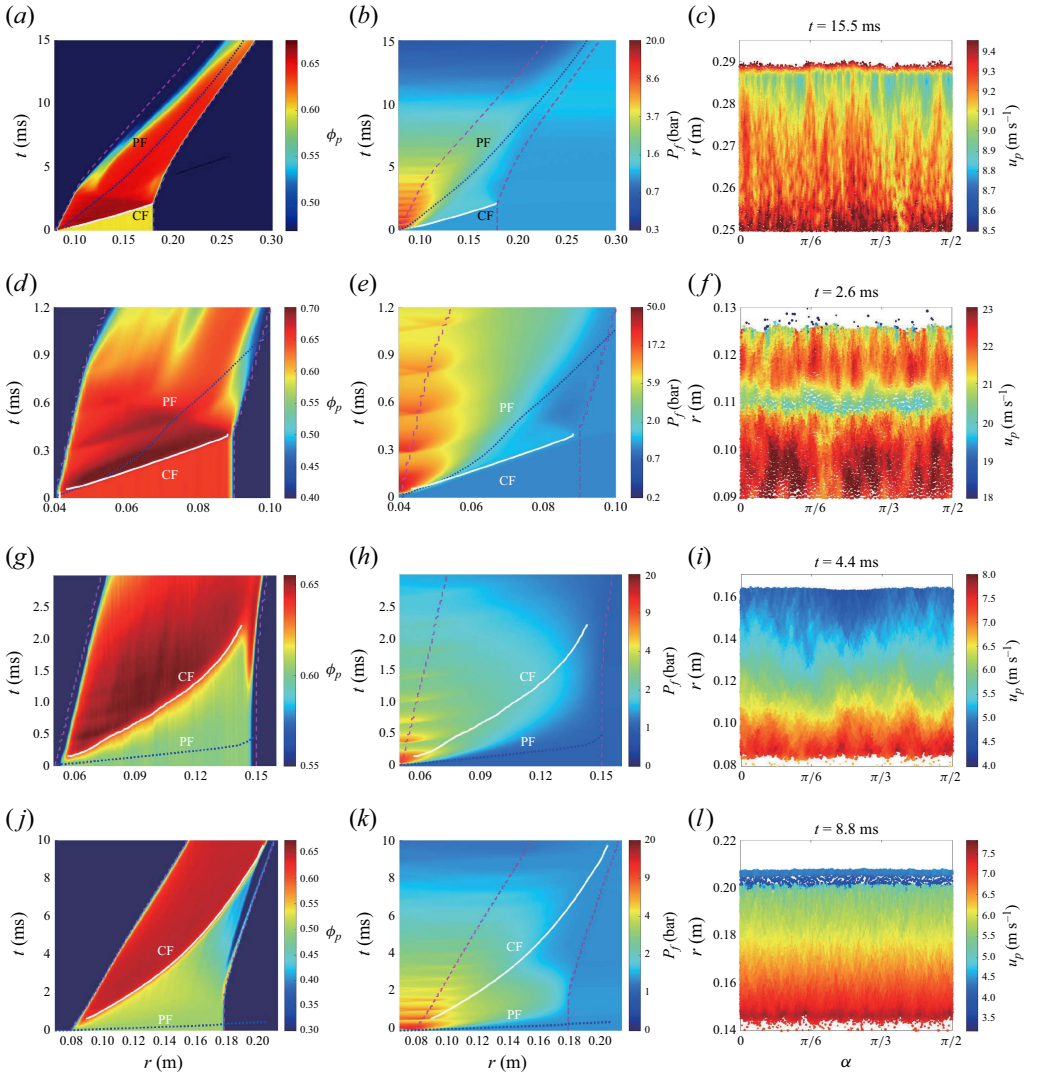


Figure 22. Simulated r–t diagrams of $\phi_p(r,t)$, (a,d,g,j), gas pressure P_f, (b,e,h,k) and particle velocity fields $u_p(r,\alpha)$, (f,i,l), in case 113 (a,b,c), case 35 (d,e,f), case 67 (g,h,i), case 12 (j,k,l). The superimposed pink trajectories are (from left to right) the inner and outer surfaces of densely packed ring ($R_{in,dense}$, R_{dense}), The superimposed white and blue trajectories denote, respectively, trajectories of the CF and PF.

by increasing ξ_{macro}. In contrast, for cases within relatively high M/C range (10^3), where the particle ring is able to decelerate and contract, lower P_0 will decrease the amplitude of ring expansion and contraction by lowering the momentum of the particle ring. In that case, lower P_0 will weaken particle jetting by decreasing ξ_{macro}.

A.3. *Early-time dynamics of the particle ring*

Section 3.3 detailed two distinct early-time dynamics of the particle ring with two cases. Here, the early-time dynamics of particle rings in more cases are presented to further demonstrate the correlation between the early-time dynamics of the particle ring and the competition between shock compaction and gas filtration. Figure 22 displays the spatial and time evolution of circumferentially averaged volume fraction ϕ_p (a,d,g,j) and gas

https://doi.org/10.1017/jfm.2025.11013 Published online by Cambridge University Press

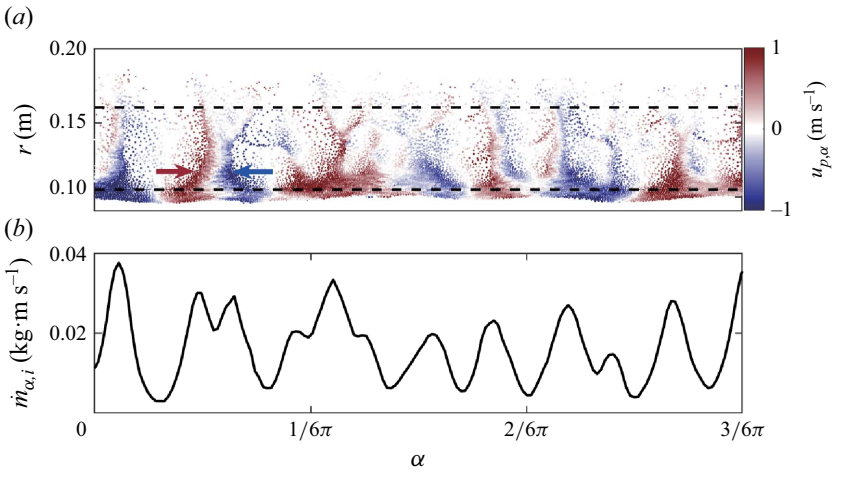


Figure 23. (*a*) Particle circumferential velocity fields, $u_{p,\alpha}$ (r, α), and (*b*) circumferential distribution curve of the particle mass flux in one quarter sector in case 1035-0.6-100-2500. Positive velocities (red) denote rightward motion and negative velocities (blue) indicate leftward motion. From bottom to top, the two dashed lines in (*a*) denote the positions of the jet root (R_{root}) and the jet tip (R_{tip}), respectively.

pressure (*b*,*e*,*h*,*k*) of four cases. For cases with CF faster than PF (case 113, case 35), the particle velocity fields $u_p(r,\alpha)$ after the refection of CF from the ring's outer surface is presented (*c*,*f*), while for cases having a CF slower than PF, the particle velocity fields $u_p(r,\alpha)$ after the full development of gas filtration is shown (*i*, *l*). As shown in figure 22, particle velocity fields of cases where CF precedes PF exhibit prominent spatial heterogeneities inherited from force-chain networks. Such heterogeneities are characterised by localised clusters of high-velocity particles. These high-velocity particle clusters at the outermost layers of the particle ring are jet precursors of jetting structures. For cases where CF lags behind PF significantly (case 67, case 12), particles at the outermost layers are initially driven by the diffusion pressure field instead of inter-particle collision. This gas-mediated momentum transfer leads to particles with relatively uniform and low velocity at outliers.

Appendix B. The definition and calculation of $\dot{\boldsymbol{M}}_{\boldsymbol{p,\alpha}}$

This appendix provides the formal definition and calculation methodology for the circumferential particle mass flux ($\dot{\boldsymbol{M}}_{\boldsymbol{p,\alpha}}$), a quantity that characterises the strength of particle migration in the circumferential direction. As illustrated in figure 23(*a*), the local circumferential velocity of particles is visualised, where positive velocities (red) denote rightward motion and negative velocities (blue) indicate leftward motion. The presence of opposing velocities across regions spanning multiple fine jets signifies particle migration toward the roots of the jets, a phenomenon that facilitates jet development. The strength of this circumferential migration is directly proportional to both the mass of the migrating particles and their annular velocity.

To compute the circumferential particle mass flux within the jet region ($R_{root} < r_i < R_{tip}$), the particle cloud region is circumferentially divided into N equal wedges with small enough circular thickness da. Every wedge is labelled by its circular coordinate α_i, and the mass flux within wedge α_i, $\dot{\boldsymbol{m}}_{\boldsymbol{\alpha},\boldsymbol{i}}$, is expressed as

$$\dot{m}_{\alpha,i} = \sum_{i=1}^{n_i} m_i \left| u_{p,\alpha,i} \right|, \tag{B1}$$

https://doi.org/10.1017/jfm.2025.11013 Published online by Cambridge University Press

where m_i is the mass of the ith particle, $u_{\alpha,i}$ is the annular velocity of the ith particle. By evaluating the mass flux for each wedge, we obtain the circumferential distribution of the particle mass flux $\dot{m}_{\alpha,i}$ (α). Figure 23(b) illustrates the circumferential distribution curve of the particle mass flux for case 1035-0.6-100-2500. To obtain the total circumferential particle mass flux within the jet region, $\dot{\boldsymbol{M}}_{\boldsymbol{p},\boldsymbol{\alpha}}$, the summation is performed circumferentially.

Here, n_i is the total number of particles within wedge α_i ($\alpha_i \leq a < \alpha_i + d\alpha$, $R_{root} < r_i < R_{tip}$)

$$\dot{M}_{p,\alpha} = \sum_{i=1}^{N} \dot{m}_{\alpha,i} = \sum_{i=1}^{N} \sum_{i=1}^{n_i} m_{\alpha,i} \left| u_{p,\alpha,i} \right| . \tag{B2}$$

Appendix C. Full formulations of governing equations for theoretical model

C.1. *Gas filtration and central gases' evolution*

The configuration of the archetype, as illustrated in figure 1(a), consists of a circular central gas pocket with an initial radius $R_{in,0}$. This pocket is filled with homogeneous static gases characterised by an initial pressure P_0, temperature T_0 and density $\rho_{centre,0}$. These quantities are related through the ideal gas law

$$\rho_{centre,0} = \frac{P_0}{\overline{R} T_0}, \tag{C1}$$

where the specific gas constant is denoted by $\overline{R} = 288.7\text{J kg}^{-1}\ \text{k}^{-1}$. The enclosing ring, with initial inner and outer radii $R_{in,0}$ and $R_{out,0}$, respectively, is composed of a compressible porous medium with an initial porosity ϵ_0 and solid phase density ρ_{solid}.

During the shock compaction and subsequent ring pulsation phases, gases in the central gas pocket are allowed to flow outward (when the central pressure is positive) or inward (when the central pressure is negative) due to inter-pore gas filtration. This process is governed by the Forchheimer equation

$$\frac{\mathrm{d}P_{gas}}{\mathrm{d}r} = -\frac{\mu}{k}\varepsilon \left(u_{gas} - u_{solid}\right) - \beta \rho_{\text{gas}} \left(u_{gas} - u_{solid}\right) \left| u_{gas} - u_{solid} \right| . \tag{C2}$$

(i) P_{gas} is the gas pressure;
(ii) u_{solid} and u_{gas} are the velocities of the solid and gas phases, respectively;
(iii) ϵ is the local porosity;
(iv) μ is the dynamic viscosity of the interstitial gases;
(v) k is the permeability, which is a function of the local porosity ϵ and particle radii d_p, as described by the Ergun expression

$$k = \frac{1}{150} \frac{\varepsilon^3}{(1-\varepsilon)^2} d_p^2. \tag{C3}$$

(i) The parameter β is the inertial resistance coefficient.

$$\beta = 1.8 \frac{1-\varepsilon}{\varepsilon} \frac{1}{d_p}. \tag{C4}$$

https://doi.org/10.1017/jfm.2025.11013 Published online by Cambridge University Press

The diffusional pressure field, P_{gas}, is governed by the Morrison equation in polar coordinates

$$\frac{\partial\left(\varepsilon P_{gas}\right)}{\partial t}=-\frac{\partial\left[\varepsilon\left(u_{gas}-u_{solid}\right)P_{gas}r\right]}{r\partial r}. \tag{C5}$$

The boundary conditions for (C5) are set by the pressures on the inner and outer surfaces of the ring: $P_{gas}\left(R_{in}\right)=P_{centre}$ and $P_{gas}\left(R_{out}\right)=P_{amb}$. Here, P_{centre} is the gas pressure within the central gas pocket.

The mass loss or gain rate of the central gases depends on the gas velocity at the inner surface of the ring relative to the moving inner surface

$$\dot{m}_{gas}\left(t\right)=2\pi R_{in}\cdot\rho_{gas}\left(R_{in}\right)\cdot\left[u_{gas}\left(R_{in}\right)-V_{in}\right]\cdot\varepsilon\left(R_{in}\right), \tag{C6}$$

where V_{in} is the expansion velocity of the inner surface, $V_{in}=u_{solid}\left(R_{in}\right)$. The instantaneous mass retained inside the central gas pocket is given by

$$m_{gas}\left(t\right)=m_{gas,0}-\int_0^t\dot{m}_{gas}\mathrm{d}t, \tag{C7}$$

where $m_{gas,0}=\pi R^2{}_{in,0}\cdot\rho_{centre,0}$ is the initial mass of the central gases. The cumulative mass flux, combined with the volumetric variation of the central gas pocket due to ring expansion or implosion, leads to the density evolution of the central gases

$$\begin{aligned}\rho_{centre}&=\frac{R^2{}_{in,0}}{R^2{}_{in}}\rho_{centre,0}-\int_0^t\frac{2\rho_{gas}\left(R_{in}\right)}{R_{in}}\cdot\left[u_{gas}\left(R_{in}\right)-V_{in}\right]\cdot\varepsilon\left(R_{in}\right)\mathrm{d}t\\&=\frac{R^2{}_{in,0}}{R^2{}_{in}}\rho_{centre,0}+\int_0^t\frac{2\rho_{gas}\left(R_{in}\right)}{R_{in}}\cdot\frac{k}{\mu}\nabla P_{R_{in}}\mathrm{d}t.\end{aligned} \tag{C8}$$

Assuming an isentropic expansion for the central gases, we obtain

$$\frac{P_{centre}}{\rho_{centre}^{\gamma}}=\frac{P_0}{\rho_{centre,0}^{\gamma}}, \tag{C9}$$

where γ is the specific heat ratio, $\gamma=1.4$. Substituting (C1) and (C8) into (C9) yields the instantaneous central pressure, which also acts as the pressure on the inner surface of the ring: $P_{gas}\left(R_{in}\right)=P_{centre}$

$$P_{gas}\left(R_{in}\right)=P_{centre}=\frac{\overline{R}^{\gamma}T_0^{\gamma}}{P_0^{\gamma-1}}\cdot\left[\frac{R^2{}_{in,0}}{R^2{}_{in}}\frac{P_0}{\overline{R}T_0}+\int_0^t\frac{2\rho_{gas}\left(R_{in}\right)}{R_{in}}\cdot\frac{k}{\mu}\nabla P_{R_{in}}\mathrm{d}t\right]^{\gamma}. \tag{C10}$$

As seen in (C10), the P_{centre} depends on both the ring dynamics and gas filtration. The former dictates the volumetric variation of the central gas pocket via R_{in} and ϵ. while the latter involves dynamic flow parameters such as $u_{gas}\left(R_{in}\right)$ and $\rho_{gas}(R_{in})$.

Since the evolutions of the central gases (C10), gas filtration (C2), the diffusional pressure field (C5) and the ring dynamics are coupled, their governing equations must be solved simultaneously.

C.2. *Shock-compaction submodel*

Upon the release of the pressurised central gases, a diffusional pressure field develops across the ring thickness and propagates outward, as shown in figure 24(*a*). Simultaneously, interstitial gases begin to flow, driven by the diffusional pressure field. The solid phase of the ring, immersed in this advancing pressure field, is subjected to an outward pressure gradient force $F_{\nabla P}$ and an associated drag force F_{drag}, both of which

https://doi.org/10.1017/jfm.2025.11013 Published online by Cambridge University Press

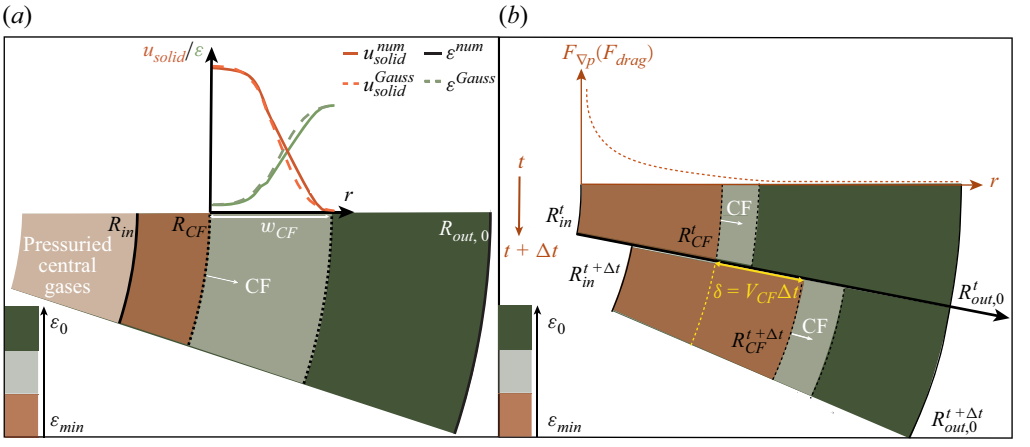


Figure 24. Schematics of configuration considered in the theoretical model. (*a*) A CF has a finite thickness of w_{CF} across which the porosity ϵ and solid velocity u_{solid} gradually decrease. (*b*) Propagation of the CF with a velocity of V_{CF} driven by the F_{∇_P} and F_{drag}. The radial profiles of ϵ (r), $u_{solid}(r)$, $F_{\nabla_P}(r)$ and $F_{drag}(r)$ are superimposed in the plots.

scale with the local pressure gradient

$$F_{\nabla P} = -\frac{\mathrm{d}P_{gas}/\mathrm{d}r}{\rho_{solid}}, \tag{C11}$$

$$F_{drag} = \frac{\varepsilon}{1-\varepsilon} F_{\nabla P} = -\frac{\varepsilon}{1-\varepsilon}\frac{\mathrm{d}P_{gas}/\mathrm{d}r}{\rho_{solid}}. \tag{C12}$$

These forces compact the solid skeleton into a compacted band with a minimum porosity $\epsilon_{min} = 0.3$. The compacted band extends from the inner surface of the ring to a CF, as illustrated in figure 24(*a*). Ahead of the CF, a transitional zone with a finite thickness $w_{CF} \sim 10d_p$ exists, across which 1-ϵ and u_{solid} gradually decrease from 1-ϵ_{min} and $u_{solid}(R_{CF})$ to 1-ϵ_0 and zero, respectively. To approximate the variations in ϵ and u_{solid} within the transitional zone, a Gauss error function is employed

$$\varepsilon\,(r) = 1 - \frac{\varepsilon_{min}+\varepsilon_0}{2} + \frac{\varepsilon_{min}-\varepsilon_0}{2}\cdot erf\left(4\frac{r-R_{CF}}{w_{CF}}\right),\ R_{CF} \le r \le R_{CF}+w_{CF}, \tag{C13}$$

$$u_{solid}\,(r) = \frac{u_{solid,CF}}{2} - \frac{u_{solid,CF}}{2}\cdot erf\left(4\frac{r-R_{CF}}{w_{CF}}\right),\ R_{CF} \le r \le R_{CF}+w_{CF}, \tag{C14}$$

$$erf\,(x) = \frac{2}{\sqrt{\pi}}\int_0^x e^{-\eta^2}\mathrm{d}\eta, \tag{C15}$$

where $u_{solid,CF} = u_{solid}(R_{CF})$. The profiles of $\epsilon(r)$ and $u_{solid}(r)$ described by (C13) and (C14) agree well with numerically derived profiles, as shown in figure 24(*a*).

The momentum balance of the annular compacted band, as demonstrated in figure 24(*b*), is given by

$$\begin{aligned}\rho_{solid}\,(1-\varepsilon_{min})\int_{R_{in}}^{R_{CF}} \dot{u}_{solid}\,(r)\,r\mathrm{d}r = &-\rho_{solid}\,(1-\varepsilon_0)\,u_{solid,CF}V_{CF}R_{CF}\\ &+\rho_{solid}\,(1-\varepsilon_{min})\int_{R_{in}}^{R_{CF}} F_{\nabla P}\,r\mathrm{d}r\\ &+\rho_{solid}\,(1-\varepsilon_{min})\int_{R_{in}}^{R_{CF}} F_{drag}\,r\mathrm{d}r,\end{aligned} \tag{C16}$$

https://doi.org/10.1017/jfm.2025.11013 Published online by Cambridge University Press

where $\dot{u}_{solid}$ denotes the acceleration of the solid phase. The first term on the right-hand side of (C16) accounts for the increase in mass within the compacted band. The second and third terms on the right-hand side represent the total pressure gradient force and the total drag force, respectively, acting on the compacted band per unit cross-sectional area. The mass conservation of the incompressible compacted band requires that u_{solid} is proportional to $1/r$

$$u_{solid}\,(r) = \frac{V_{in}R_{in}}{r},\ R_{in} \le r \le R_{CF}. \tag{C17}$$

Differentiating (C17) yields the acceleration of the solid phase

$$\dot{u}_{solid}\,(r) = \frac{\dot{V}_{in}R_{in}}{r} + \frac{V_{in}^2}{r} - \frac{(V_{in}R_{in})^2}{r^3},\ R_{in} \le r \le R_{CF}. \tag{C18}$$

At the CF, the following conditions hold:

$$u_{solid,CF} = \frac{V_{in}R_{in}}{R_{CF}}, \tag{C19}$$

$$\dot{u}_{solid,CF} = \frac{\dot{V}_{in}R_{in}}{R_{CF}} + \frac{V_{in}^2}{R_{CF}} - \frac{(V_{in}R_{in})^2}{R_{CF}^3}. \tag{C20}$$

The velocities V_{CF} and V_{in} must satisfy the Rankine–Hugoniot condition

$$V_{in} = \frac{V_{CF}R_{CF}}{R_{in}}\left(\frac{\varepsilon_0 - \varepsilon_{min}}{1 - \varepsilon_{min}}\right). \tag{C21}$$

Equations (C16)–(C21) constitute the complete set of governing equations for the shock compaction of the solid phase, which is coupled to the evolution of interstitial gas flows.

C.3. *Ring pulsation submodel*

Once the CF reaches the outer surface of the ring, the ring dynamics transitions to the ring pulsation phase, synchronised with the fluctuation of the central pressure. The ring is treated as incompressible, with a constant porosity $\epsilon = e_{min}$. The momentum balance of the ring as a whole is expressed as

$$\rho_{solid}\,(1-\varepsilon_{min})\int_{R_{in}}^{R_{out}} r\dot{u}_{solid}\mathrm{d}r = \rho_{solid}\,(1-\varepsilon_{min})\int_{R_{in}}^{R_{out}} F_{\nabla P}\cdot r\,\mathrm{d}r + \rho_{solid}\,(1-\varepsilon_{min})\int_{R_{in}}^{R_{out}} F_{drag}\cdot r\,\mathrm{d}r. \tag{C22}$$

Similar to (C16), the first and second terms on the right-hand side of (C22) represent the total pressure gradient force and the total drag force, respectively, acting on the ring per unit cross-sectional area. The parameters F_{∇_P} and F_{drag} are described by (C11) and (C12), respectively. Due to the incompressibility of the ring, we have

$$u_{solid}\,(r) = \frac{V_{in}R_{in}}{r},\ R_{in} \le r \le R_{out}, \tag{C23}$$

$$\dot{u}_{solid}\,(r) = \frac{\dot{V}_{in}R_{in}}{r} + \frac{V_{in}^2}{r} - \frac{(V_{in}R_{in})^2}{r^3},\ R_{in} \le r \le R_{out}. \tag{C24}$$

https://doi.org/10.1017/jfm.2025.11013 Published online by Cambridge University Press

Integrating $\dot{u}_{solid}$ from the inner to the outer surface of the ring yields

$$\int_{R_{in}}^{R_{out}} \dot{u}_{solid}\, r\mathrm{d}r = \int_{R_{in}}^{R_{out}} \left(\dot{V}_{in} R_{in} + V_{in}^2 - V_{in}^2 \frac{R_{in}^2}{r^2} \right) \mathrm{d}r$$
$$= \dot{V}_{in} R_{in} \left(R_{out} - R_{in} \right) + V_{in}^2 \frac{\left(R_{out} - R_{in} \right)^2}{R_{out}}. \tag{C25}$$

Substituting (C11), (C12) and (C25) into (C22) reduces the momentum balance to

$$\left(R_{out} - R_{in} \right) \rho_{solid} \left[\dot{V}_{in} R_{in} + V_{in}^2 \left(1 - \frac{R_{in}}{R_{out}} \right) \right] = -\frac{1}{1 - \varepsilon_{min}} \int_{R_{in}}^{R_{out}} d P_{gas}/\mathrm{d}r \cdot r\mathrm{d}r. \tag{C26}$$

Equations (C23), (C24) and (C26) constitute the key governing equations for the ring dynamics in the ring pulsation submodel. The evolution of the central gases and gas filtration through the ring occur concurrently.

References

Baer, M.R. & Nunziato, J.W. 1986 A two-phase mixture theory for the deflagration-to-detonation transition (ddt) in reactive granular materials. *Intl J. Multiphase Flow* **12**, 861–889.

Bai, C.H., Wang, Y., Xue, K. & Wang, L.F. 2018 Experimental study of detonation of large-scale powder–droplet–vapor mixtures. *Shock Waves* **28**, 599–611.

Bajpai, A., Wangikar, A.U., Tewari, C. & Kumar, R. 2025 Computational investigation of moving shock interaction with a granular particle curtain using a coupled Eulerian–Lagrangian approach. *Phys. Fluids* **37**, 013374.

Balakrishnan, K. 2014 Explosion-driven Rayleigh–Taylor instability in gas-particle mixtures. *Phys. Fluids* **26**, 043303.

Beetstra, R., Hoef, M.A.V.D. & Kuipers, J.A.M. 2007 Drag force of intermediate reynolds number flow past mono-and bidisperse arrays of spheres. *AIChE J.* **53**, 489–501.

Borg, J.P. & Vogler, T.J. 2008 Mesoscale calculations of the dynamic behavior of a granular ceramic. *Intl J. Solids Struct.* **45**, 1676–1696.

Borg, J.P. & Vogler, T.J. 2013 Rapid compaction of granular material: characterizing two- and three-dimensional mesoscale simulations. *Shock Waves* **23**, 153–176.

Britan, A. & Ben-Dor, G. 2006 Shock tube study of the dynamical behavior of granular materials. *Intl J. Multiphase Flow* **32**, 623–642.

Chen, X., Wang, Z. & Liu, Y. 2020 A whole explosive dispersion process prediction model for fuel clouds. *Propellants Explosives Pyrotechnics* **45**, 950–965.

Chiapolino, A. & Saurel, R. 2020 Numerical investigations of two-phase finger-like instabilities. *Comput. Fluids* **206**, 104585.

Crowl, D.A. 2003 *Understanding Explosions*. Understanding Explosions.

Daniel, K.A. & Wagner, J.L. 2022 The shock-induced dispersal of particle curtains with varying material density. *Intl J. Multiphase Flow* **152**, 104082.

Demauro, E.P., Wagner, J.L., Dechant, L.J., Beresh, S.J. & Turpin, A.M. 2019 Improved scaling laws for the shock-induced dispersal of a dense particle curtain. *J. Fluid Mech.* **876**, 881–895.

Di Felice, R. 1994 The voidage function for fluid-particle interaction systems. *Intl J. Multiphase Flow* **20**, 153–159.

Duke-Walker, V., Maxon, W.C., Almuhna, S.R. & McFarland, J.A. 2021 Evaporation and breakup effects in the shock-driven multiphase instability. *J. Fluid Mech.* **908**, A13.

Frost, D.L. 2018 Heterogeneous/particle-laden blast waves. *Shock Waves* **28**, 439–449.

Frost, D.L., Grégoire, Y., Petel, O., Goroshin, S. & Zhang, F. 2012 Particle jet formation during explosive dispersal of solid particles. *Phys. Fluids* **24**, 091109.

Frost, D.L., Loiseau, J., Goroshin, S., Fan, Z., Milne, A. & Longbottom, A. 2017 Fracture of explosively compacted aluminum particles in a cylinder. *AIP Conf. Proc.* **1793**, 1–6.

Gregoire, Y. 2012 Development of instabilities in explosively dispersed particles. In *Shock Compression of Condensed Matter - 2011, PTS 1 and 2*, vol. 1426, pp. 1623.

Han, P. & Xue, K. 2025 Shock attenuation of dense granular media. *J. Fluid Mech.* **1009**, A22.

https://doi.org/10.1017/jfm.2025.11013 Published online by Cambridge University Press

HAOYANG, L. & DU, Z. 2024 Study on the development of aerial fire extinguishing munition for forest fires and fire extinguishing tests. *Case Stud. Therm. Engng* **55**, 104138.
KONERU, R.B., ROLLIN, B., DURANT, B., OUELLET, F. & BALACHANDAR, S. 2020 A numerical study of particle jetting in a dense particle bed driven by an air-blast. *Phys. Fluids* **32**, 093301.
LING, Y., PARMAR, M. & BALACHANDAR, S. 2013 A scaling analysis of added-mass and history forces and their coupling in dispersed multiphase flows. *Intl J. Multiphase Flow* **57**, 102–114.
LIU, X.D., OSHER, S. & CHAN, T. 1994 Weighted essentially non-oscillatory schemes. *J. Comput. Phys.* **115**, 200–212.
LOISEAU, J., PONTALIER, Q., MILNE, A.M., GOROSHIN, S. & FROST, D.L. 2018 Terminal velocity of liquids and granular materials dispersed by a high explosive. *Shock Waves* **28**, 473–487.
MEHTA, Y., NEAL, C., SALARI, K., JACKSON, T.L., BALACHANDAR, S. & THAKUR, S. 2018 Propagation of a strong shock over a random bed of spherical particles. *J. Fluid Mech.* **839**, 157–197.
MIAO, L., LI, J. & XUE, K. 2024 Multiscale understanding of structural effect on explosive dispersal of granular media. *J. Fluid Mech.* **999**, A46.
MILNE, A.M., FLOYD, E., LONGBOTTOM, A.W. & TAYLOR, P. 2014 Dynamic fragmentation of powders in spherical geometry. *Shock Waves* **24**, 501–513.
NARBONA-REINA, G., BRESCH, D., BURGISSER, A. & COLLOMBET, M. 2024 Two-phase magma flow with phase exchange: part I. Physical modeling of a volcanic conduit. *Stud. Appl. Math.* **153**, 1–85.
OSNES, A.N., VARTDAL, M., OMANG, M.G. & REIF, B.A.P. 2020 Particle-resolved simulations of shock-induced flow through particle clouds at different Reynolds numbers. *Phys. Rev. Fluids* **5**, 014305.
OSNES, A.N., VARTDAL, M. & PETTERSSON REIF, B.A. 2018 Numerical simulation of particle jet formation induced by shock wave acceleration in a Hele-Shaw cell. *Shock Waves* **28**, 451–461.
OUELLET, F., ROLLIN, B., DURANT, B., KONERU, R.B. & BALACHANDAR, S. 2022 Shock-driven dispersal of a corrugated finite-thickness particle layer. *Phys. Fluids* **34**, 083301.
PARMAR, M., HASELBACHER, A. & BALACHANDAR, S. 2009 Modeling of the unsteady force for shock–particle interaction. *Shock Waves* **19**, 317–329.
PONTALIER, Q., LOISEAU, J., GOROSHIN, S. & FROST, D.L. 2018 Experimental investigation of blast mitigation and particle–blast interaction during the explosive dispersal of particles and liquids. *Shock Waves* **28**, 489–511.
RIPLEY, R.C. & ZHANG, F. 2014 Jetting instability mechanisms of particles from explosive dispersal. *J. Phys.: Conf. Series* **500**, 152012.
RITZEL, D.V., RIPLEY, R.C., MURRAY, S.B. & ANDERSON, J. 1888 Near-field blast phenomenology of thermobaric explosions. In *Shock Waves*, pp. 305–310.
RODRIGUEZ, V., SAUREL, R., JOURDAN, G. & HOUAS, L. 2013 Solid-particle jet formation under shock-wave acceleration. *Phys. Rev. E: Statist. Nonlinear Soft Matt. Phys.* **88**, 1–6.
RODRIGUEZ, V., SAUREL, R., JOURDAN, G. & HOUAS, L. 2014 External front instabilities induced by a shocked particle ring. *Phys. Rev. E.* **90**, 043013.
RODRIGUEZ, V., SAUREL, R., JOURDAN, G. & HOUAS, L. 2017 Impulsive dispersion of a granular layer by a weak blast wave. *Shock Waves* **27**, 187–198.
ROGUE, X., RODRIGUEZ, G., HAAS, J.F. & SAUREL, R. 1998 Experimental and numerical investigation of the shock-induced fluidization of a particles bed. *Shock Waves* **8**, 29–45.
SEO, D., LUSCHER, D.J., SCOVEL, C. & DAPHALAPURKAR, N.P. 2024 Mesoscale simulation of granular materials under weak shock compaction–pore size distribution effects. *J. Appl. Phys.* **136**, 155902.
SUGIYAMA, Y., ANDO, H., SHIMURA, K. & MATSUO, A. 2019 Numerical investigation of the interaction between a shock wave and a particle cloud curtain using a CFD–DEM model. *Shock Waves* **29**, 499–510.
SUNDARESAN, S., OZEL, A. & KOLEHMAINEN, J. 2018 Toward constitutive models for momentum, species, and energy transport in gas–Particle flows. *Annu. Rev. Chem. Biomol.* **9**, 61–81.
TENNETI, S., GARG, R. & SUBRAMANIAM, S. 2011 Drag law for monodisperse gas-solid systems using particle-resolved direct numerical simulation of flow past fixed assemblies of spheres. *Intl J. Multiphase Flow* **37**, 1072–1092.
TIAN, B., ZENG, J., MENG, B., CHEN, Q., GUO, X. & XUE, K. 2020 Compressible multiphase particle-in-cell method (CMP-PIC) for full pattern flows of gas-particle system. *J. Comput. Phys.* **418**, 1.
TÜRKER, L. 2016 Thermobaric and enhanced blast explosives (TBX and EBX). *Defence Techn.* **12**, 423–445.
VOROBIEFF, P., ANDERSON, M., CONROY, J., WHITE, R., TRUMAN, C.R. & KUMAR, S. 2011 Vortex formation in a shock-accelerated gas induced by particle seeding. *Phys. Rev. Lett.* **106**, 184503.
WAGNER, J., BERESH, S., KEARNEY, S., TROTT, W., CASTANEDA, J., PRUETT, B. & BAER, M. 2012 A multiphase shock tube for shock wave interactions with dense particle fields. *Exp. Fluids* **52**, 1507–1517.
XUE, K., DU, K., SHI, X., GAN, Y. & BAI, C. 2018 Dual hierarchical particle jetting of a particle ring undergoing radial explosion. *Soft Matt.* **14**, 4422–4431.

https://doi.org/10.1017/jfm.2025.11013 Published online by Cambridge University Press

XUE, K., MIU, L., LI, J., BAI, C. & TIAN, B. 2023 Explosive dispersal of granular media. *J. Fluid Mech.* **959**, A17.

YOO, J., KIM, J.H. & KIM, D. 2025 Shock-induced dispersion patterns of powder with diverse physical properties. *Soft Matt.* **21**, 3789–3802.

ZHANG, C., FENG, C. & XUE, K. 2023 Numerical study of blast wave propagation through granular materials subjected to buried blasts. *Powder Technol.* **429**, 118940.

ZHANG, F., RIPLEY, R.C., YOSHINAKA, A., FINDLAY, C.R., ANDERSON, J. & VON ROSEN, B. 2015 Large-scale spray detonation and related particle jetting instability phenomenon. *Shock Waves* **25**, 239–254.

ZHANG, J., MAJMUDAR, T.S., TORDESILLAS, A. & BEHRINGER, R.P. 2010 Statistical properties of a 2-D granular material subjected to cyclic shear. *Granul. Matt.* **12**, 159–172.

ZHAO, J., ZHAO, S. & LUDING, S. 2023 The role of particle shape in computational modelling of granular matter. *Nat. Rev. Phys.* **5**, 505–525.

https://doi.org/10.1017/jfm.2025.11013 Published online by Cambridge University Press